Influence of mass-ratio corrections in extreme-mass-ratio inspirals for testing general relativity

Ping Shen,[1,2] Wen-Biao Han,[3,1,2,4,*] Chen Zhang,[1] Shu-Cheng Yang,[1] Xing-Yu Zhong,[1,2] Ye Jiang,[1,2] and Qiuxin Cui[5]

[1]*Shanghai Astronomical Observatory, Shanghai 200030, China*
[2]*School of Astronomy and Space Science, University of Chinese Academy of Sciences, Beijing 100049, China*
[3]*School of Fundamental Physics and Mathematical Sciences, Hangzhou Institute for Advanced Study, UCAS, Hangzhou 310024, China*
[4]*Shanghai Frontiers Science Center for Gravitational Wave Detection, 800 Dongchuan Road, Shanghai 200240, China*
[5]*Department of Astronomy, University of Science and Technology of China, Hefei 230026, China*

(Received 21 March 2023; accepted 12 July 2023; published 8 September 2023)

The popular waveform templates of extreme-mass-ratio inspirals usually omit the mass-ratio corrections in conservative dynamics, and employ adiabatic approximation to include the radiation reaction. With the help of effective-one-body dynamics, we investigate the influence of mass-ratio corrections in the conservative part on the gravitational waves. We find that for the extra-relativistic orbits, the mass-ratio corrections can produce obvious orbital dephasing even for a very small mass ratio and then affect the waveforms. More importantly, it is noted that omitting the mass-ratio corrections in waveform templates may induce a fake signal of deviation from general relativity.

DOI: 10.1103/PhysRevD.108.064015

I. INTRODUCTION

Extreme-mass-ratio inspirals (EMRIs) [1,2], consisting of a stellar-mass compact object [SCO: white dwarf, neutron star, or black hole (BH)] inspiraling into a supermassive black hole (SMBH), are the prime sources of the space-borne gravitational wave (GW) detectors, such as the Laser Interferometer Space Antenna (LISA) [3], Taiji [4,5], and TianQin [6].

EMRIs are very important in astrophysics, cosmology, and basic physics. In astrophysics, EMRIs will provide us with relevant information on stellar dynamics in galactic nuclei, from which we can infer the formation mechanism of EMRIs [1,7–9]. In cosmology, the detection of a single EMRI event and its electromagnetic counterpart can provide an accurate measurement of the luminosity distance and the redshift to estimate the Hubble constant [10–13]. For basic physics, EMRIs can be used to test general relativity (GR) and the nature of BHs in the strong-field regime [14,15]. As an extreme mass ratio, SCO may be considered approximately as a test particle in the background of the central SMBH. The emitted GWs reflect the space-time information of the central object. If extracting this information from the gravitational-wave signals, we can accurately distinguish whether the central object is a Kerr BH or another corresponding object.

Extensive work has been done to quantify the ability of space-based GW detectors (LISA, Taiji, TianQin, etc.) to measure the deviation of multipole moments from the Kerr BH and then test GR [15–19]. In particular, all of the multipoles of Kerr BH are determined by its mass $M_0 = M$ and spin $S_1 = J = Ma$:

$$M_l + iS_l = M(ia)^l, \tag{1}$$

where M_l and S_l are the mass and mass-current multipole moments, respectively, and a is the standard Kerr spin parameter. For example, Ryan found that for a simplified case of circular, equatorial orbits, a LISA observation can measure the mass quadrupole moment to the accuracy of $\Delta M_2/M^3 \sim 0.0015$–$0.015$ [16]. Barack and Cutler extended Ryan's work to generic orbits and considered the modulations caused by satellite motions [15]. Collins and Hughes constructed the space-time of bumpy BHs, which are similar to the Kerr BH, but with different multipoles. If the BH candidates are indeed Kerr BHs in GR, then their bumps should be zero [17]. Furthermore, Kwinten Fransen and Daniel R. Mayerson estimated the accuracy of LISA EMRIs to measure the equatorial symmetry breaking using the lowest-lying odd-parity multipole moments S_2 and M_3. They found that S_2/M^3 will typically be detectable with a measurement accuracy of $\Delta(S_2/M^3) \approx 1\%$ [18].

*wbhan@shao.ac.cn

These tests require an accurate waveform template. With the accumulation of observation time from several months to a few years, the signal-to-noise ratio (SNR) of EMRIs could become large enough to be detected by matched filtering [1]. However, the accuracy of the waveform template is also expected to be very high to detect such long-duration signals and extract the source parameters. For detection purposes, it is required that the dephasing over the signal's duration should be less than a few radians. For source parameter extraction, the dephasing should satisfy $\Delta\phi \lesssim 1/\mathrm{SNR}$ [2,20]. As in Ref. [21], the GW phase ϕ can be expanded as

$$\phi = \nu^{-1}\phi_0 + \nu^0\phi_1 + O(\nu), \tag{2}$$

where ν is the mass ratio. The first term is the "adiabatic" term, i.e., the zeroth postadiabatic (0PA) term, which involves the dissipative part of the first-order self-force (1SF). The second term is the first postadiabatic (1PA) term, involving the conservative part of the 1SF and the dissipative part of the second-order self-force (2SF), which is required for exact EMRI models [22,23]. Models that get ϕ_0 might be enough to detect most signals, but models that get both ϕ_0 and ϕ_1 should be enough for precise parameter extraction [24].

Currently, there is a relatively accurate method based on the black hole perturbation theory (BHPT), i.e., the waveform can be obtained by solving the Teukolsky equation [25]. This method is based on frequency domain decomposition and treats the SCO as a test particle. The ongoing gravitational self-force (GSF) program [21] is a specific expansion within BHPT that aims to generate EMRI waveforms satisfying the requirements of the EMRI science. In this approach, EMRI is treated as a point mass orbiting a black hole, and the dynamics can be described by the equation of motion of the mass, including the influence of the interaction with the self-field, i.e., the GSF [26]. Among the GSF formalisms, the recent postadiabatic (PA) waveforms [23] are the most accurate waveforms to date. Some other methods, such as the kludge models [27,28], adiabatic waveforms [29,30], and the effective-one-body (EOB) formalism [31–35], make it possible to efficiently calculate a large number of relatively accurate waveforms.

Nowadays, kludge waveforms have been greatly developed, like analytical kludge [27], numerical kludge [28], augmented analytical kludge (AAK) [36], etc. These kludge models can generate waveforms more quickly than using the Teukolsky equation or the GSF method, and are often used for EMRI data analysis. However, they are less accurate because they represent approximations to the 0PA (adiabatic) waveforms [23]. They regard SCOs as test particles in the orbital evolution using the matched asymptotic expansions [37], ignoring the mass-ratio corrections in the conservative dynamics, which is related to the conservative part of the 1SF. However, in the future, we can incorporate the 1PA term into these waveform templates to model EMRIs exactly. While not being enough for parameter estimation, models like the AAK might be sufficient for detection, and they have been heavily used for many LISA measurement studies.

Hughes [30] *et al.* computed adiabatic (0PA) waveforms for EMRIs by "stitching" together a long inspiral waveform from a sequence of waveform snapshots, each of which corresponds to a particular geodesic orbit. But some effects are neglected by this adiabatic approximation, such as the conservative self-force and spin-curvature coupling. However, we can extend this framework to include these effects beyond the adiabatic approximation in the future. Recently, Wardell [23] *et al.* produced the 1PA waveforms for nonspinning compact binaries undergoing a quasicircular inspiral, which will be invaluable to accurately model EMRIs for the LISA mission.

As in Eq. (2), the 1PA contribution is non-negligible for all mass ratios, and the 1PA term is both necessary and sufficient for EMRI modeling [21–23]. So the lack of a 1PA term will lead to inaccurate waveform templates, which may give rise to some errors in GW parameter estimation [38,39]. In particular, using a waveform template that is not accurate enough can lead to the detection of a spurious signal deviating from the Kerr black hole case. Based on a simple linearized analysis and Fisher matrix calculations, Moore [40] *et al.* estimated the waveform errors accumulated among GW events. They found that the evidence for the deviation from GR grows as the catalog size increases. Qian Hu and John Veitch [41] investigated the impacts of overlapping signals and inaccurate waveform models on tests of GR. They confirmed that systematic errors could accumulate when combining multiple GW events and could lead to a false deviation from GR in some cases.

In our work, we are interested in evaluating the impact of inaccurate waveforms due to ignoring mass-ratio corrections (associated with the 1PA term), which may mistakenly lead to fake deviations from GR in parameter estimation. In other words, even if GR is a correct description of nature, there is a risk of making a wrong judgment on the test of gravity theory if a mass-ratio correction is ignored in waveform templates.

In the previous papers, taking advantage of the EOB formalism [31–35], some of us discussed the influence of mass-ratio corrections in conservative dynamics [42,43]. In the present work, we make a further and detailed investigation of mass-ratio corrections on the orbital motion (orbit, frequency, and phase) and gravitational radiation. We also show the discrepancy of the Teukolsky-based energy fluxes by using the EOB orbit and the test particle one. We generate our waveforms by the following scheme: First, we improve the hybrid scheme of fluxes proposed by Gair and Glampedakis [44] (hereafter GG) to obtain the orbital evolutions with a dissipative 1PA term. And then we

solve the EOB dynamical equations including mass-ratio corrections (conservative 1PA term) to get the orbital frequency. Finally, the waveforms are computed via the Teukolsly formalism. More importantly, based on the Bayesian analysis, we evaluate the possibility of inducing a fake signal of deviation from GR due to omitting the mass-ratio corrections in waveform templates. We find that for the case of the mass-ratio $\nu \lesssim 10^{-5}$, the mismatch between the EOB and test particle waveforms is so small that it can be ignored. However, for the case of $\nu \gtrsim 10^{-5}$, the mismatch is much larger, and there is a risk of making an incorrect judgment, namely, that we have detected a deviation from GR.

This paper is organized as follows. In Sec. II, the conservative dynamics part of analytical EOB formalism which includes the first-order mass-ratio corrections is introduced in detail. In Sec. III, considering the gravitational radiation, we introduce the Teukolsky equation and generate the Teukolsky-based waveforms of EMRI by combining the EOB orbit and the post-Newtonian (PN) fluxes fitted by the Teukolsky one. In Sec. IV, we consider EMRI models with different mass-ratios and SNRs to illustrate the waveform mismatches using the EOB orbit and the test particle one. We also calculate their Bayesian factors in favor of a GR deviation. Finally, in Sec. V, we draw the conclusions and discuss our results. Throughout this paper, we set $G = c = 1$, where G is the gravitational constant and c is the speed of light.

II. EFFECTIVE-ONE-BODY DYNAMICS

The basic idea of EOB formalism [45,46] is to simplify the conservation dynamics of the two-body problem in GR to the geodesic motion of the test particle in the reduced space-time. That is to say, the two-body problem of the SMBH with a mass m_1 and the smaller compact object with a mass m_2 is transformed into the single-body problem of the test particle with the reduced mass $\mu = m_1 m_2/(m_1+m_2)$ moving in the equivalent external metric field. This is equivalent to the post-Newtonian expansion of traditional two-body relative motion. The EOB Hamiltonian is written as follows:

$$H_{\rm EOB} = M\sqrt{1 + 2\nu(\hat{H}_{\rm eff} - 1)}, \tag{3}$$

where $M = m_1 + m_2$, $\nu = m_1 m_2/M^2 = \mu/M$, and $\hat{H}_{\rm eff} = H_{\rm eff}/\mu$, $H_{\rm eff}$ is the effective Hamiltonian. Once the expression of the Hamiltonian $H_{\rm EOB}$ is determined, the equations of motion can be written as

$$\frac{d\boldsymbol{r}}{dt} = \frac{\partial H_{\rm EOB}}{\partial \boldsymbol{P}}, \qquad \frac{d\boldsymbol{P}}{dt} = -\frac{\partial H_{\rm EOB}}{\partial \boldsymbol{r}} + \boldsymbol{F}, \tag{4}$$

where $\boldsymbol{r}$ represents the coordinate of the small compact object, and $\boldsymbol{P}$ is the momentum. We use $\boldsymbol{F}$ to denote the radiation reaction force of GW, which causes the energy and angular momentum of the two-body system to be no longer conserved. In the conservative dynamic part, GW radiation is ignored, that is, $\boldsymbol{F} = 0$.

The effective Hamiltonian is given by [42]

$$H_{\rm eff} = H_{\rm NS} + H_{\rm S} - \frac{\nu}{2r^3} S_*^2 \approx H_{\rm NS}, \tag{5}$$

where $H_{\rm S}$ and $H_{\rm NS}$ represent the Hamiltonian of the particle with and without spin, $S_* = aM(m_2/m_1)$ is the effective spin of the particle, and a is the deformed-Kerr spin parameter. $H_{\rm S}$ and S_* are small enough to be ignored within the range of error precision [47]. The deformed-Kerr metric is given by [48]

$$g^{tt} = -\frac{\Lambda_t}{\Delta_t \Sigma}, \tag{6a}$$

$$g^{rr} = \frac{\Delta_r}{\Sigma}, \tag{6b}$$

$$g^{\theta\theta} = \frac{1}{\Sigma}, \tag{6c}$$

$$g^{\phi\phi} = \frac{1}{\Lambda_t}\left(-\frac{\tilde{\omega}_{\rm fd}{}^2}{\Delta_t \Sigma} + \frac{\Sigma}{\sin^2\theta}\right), \tag{6d}$$

$$g^{t\phi} = -\frac{\tilde{\omega}_{\rm fd}}{\Delta_t \Sigma}, \tag{6e}$$

with

$$\Lambda_t = (r^2 + a^2)^2 - a^2 \Delta_t \sin^2\theta, \tag{7a}$$

$$\Delta_t = r^2\left[A(u) + \frac{a^2}{M^2}u^2\right], \tag{7b}$$

$$\Sigma = r^2 + a^2\cos^2\theta, \tag{7c}$$

$$\Delta_r = \Delta_t D^{-1}(u), \tag{7d}$$

$$\tilde{\omega}_{\rm fd} = 2aMr + \omega_1^{\rm fd}\nu\frac{aM^3}{r} + \omega_2^{\rm fd}\nu\frac{Ma^3}{r}, \tag{7e}$$

where $\omega_1^{\rm fd} = -10$, $\omega_1^{\rm fd} = 20$ [34,49,50], $u = \frac{M}{r}$, and A and D are metric potentials for the EOB formalism mentioned in Ref. [51], which are given in Appendix A. We still call the coordinate (t, r, θ, ϕ) used here the Boyer-Lindquist-type coordinate (i.e., in coordinates that reduce to Boyer-Lindquist coordinates if the quadrupole perturbation is zero, thus reducing the space-time to pure Kerr) [48].

As in Ref. [42], the orbital evolution equations can be expressed as functions of (ξ, χ, p, e, ι):

$$\dot{\xi} = -\frac{(1+e\cos\xi)^2}{epM\sin\xi}\frac{g^{rr}\hat{P}_r}{E/M(g^{tt}\hat{H}_{\rm eff} - g^{t\phi}\hat{L}_z)}, \tag{8a}$$

$$\dot{\chi} = -\frac{g^{\theta\theta}\sqrt{(a^2(1-\hat{H}^2_{\rm eff})(z_+^2 - z_-^2\cos^2\chi)}}{E/M(g^{tt}\hat{H}_{\rm eff} - g^{t\phi}\hat{L}_z)}, \tag{8b}$$

$$\dot{\phi} = \frac{g^{t\phi} - [g^{tt}g^{\phi\phi} - (g^{t\phi})^2]\frac{\hat{L}_z}{g^{tt}\hat{H}_{\rm eff} - g^{t\phi}\hat{L}_z}}{g^{tt}E/M}, \tag{8c}$$

where $\cos^2\theta = \cos^2\theta_{\rm min}\cos^2\chi = \sin^2\iota\cos^2\chi$, $r = pM/(1+e\cos\xi)$, p is the semilatus rectum, e is the eccentricity of the orbit, and ι is the orbital inclination. ξ varies from 0 to 2π corresponding to r going through a complete cycle, and χ varies from 0 to 2π corresponding to θ oscillating through its full range of motion [42]. L_z is the angular momentum in the z direction; P_θ, P_r, and P_ϕ are the polar, radial, and azimuthal angular momentum; and E is the total system energy. The expressions of these parameters are given in Appendix A [Eqs. (A6)–(A7), Eqs. (A9a)–(A9c)].

By solving the above ordinary differential equations by numerical integration, we can obtain ξ, χ, ϕ in the coordinate time t. Projecting the Boyer-Lindquist coordinate to the spherical coordinate grid, the corresponding Cartesian coordinate system is defined by

$$\tilde{x} = \frac{p\cos\phi\sqrt{1-z_-^2\cos^2\chi}}{1+e\cos\xi}, \tag{9a}$$

$$\tilde{y} = \frac{p\sin\phi\sqrt{1-z_-^2\cos^2\chi}}{1+e\cos\xi}, \tag{9b}$$

$$\tilde{z} = \frac{pz_-\cos\chi}{1+e\cos\xi}, \tag{9c}$$

where $z_- = \cos\theta_{\rm min}$.

In Fig. 1, we select four sets of parameters and compare the orbital evolution in the x-y plane for different mass

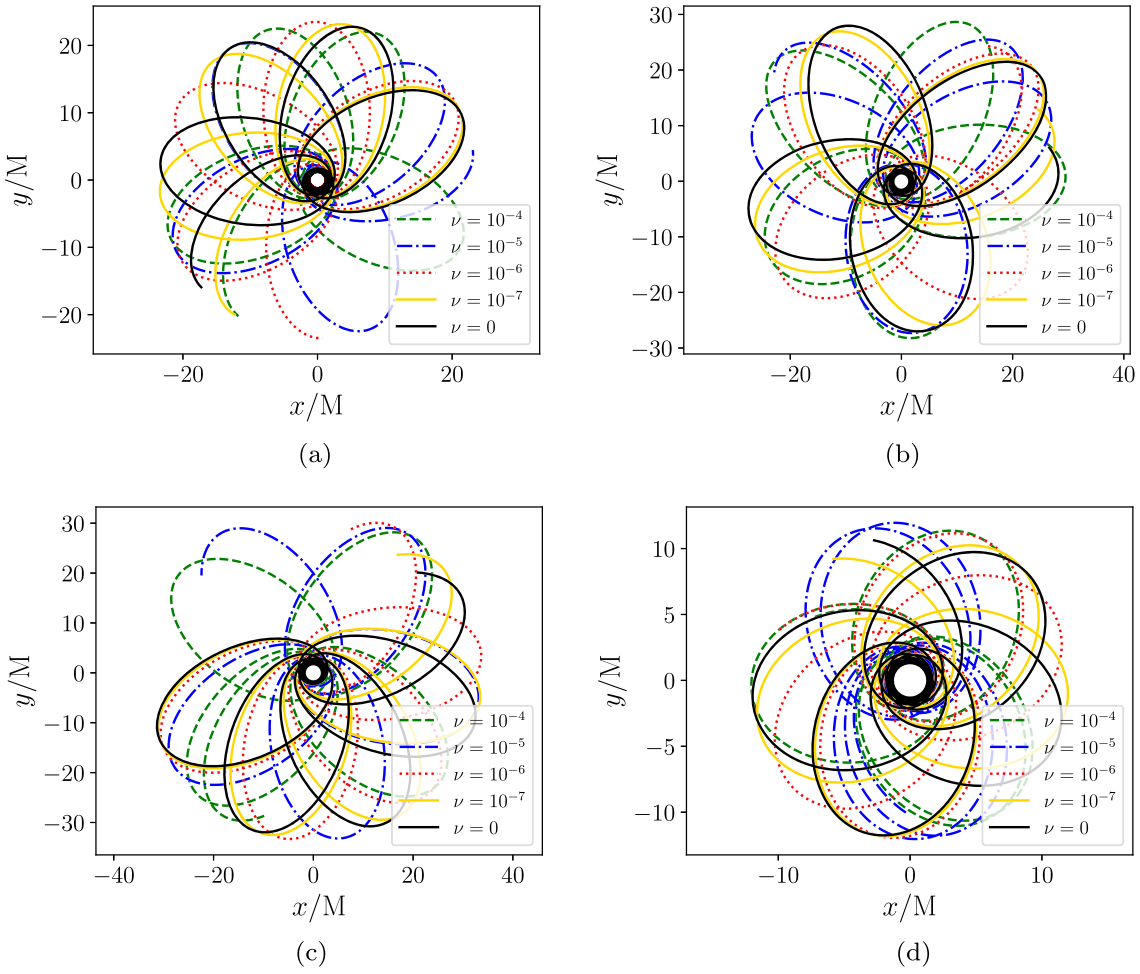

FIG. 1. Four orbits in the x-y plane of different orbital parameters. The green, blue, red, yellow, and black lines represent $\nu = 10^{-4}, 10^{-5}, 10^{-6}, 10^{-7}$, and $\nu = 0$, respectively. Note that $\nu = 0$ denotes the case of the test particle. (a) $a = 0.99, e = 0.9, \iota = 0°, p = 2.35$M; (b) $a = 0.95, e = 0.9, \iota = 30°, p = 3.15$M; (c) $a = 0.9, e = 0.9, \iota = 10°, p = 3.39$M; (d) $a = 0.98, e = 0.8, \iota = 0°, p = 2.41$M.

ratios in each group. We can see that the difference between the EOB orbit and the test particle one is obvious, especially when the mass ratio is 10^{-4} and 10^{-5}. Note that the four orbits we choose here are all zoom whirl [52]. This characteristic behavior involves several revolutions around the central body near the periastron [53], which leads to more pronounced orbital deviations than in generic orbits.

Figure 2 represents the dephasing, $\Delta\phi$, for the four orbits presented in Fig. 1. For high values of ν, the phase shift $\Delta\phi$ becomes significant. It is crucial to understand that even though the dephasing may be minor at very low values of ν ($\nu = 10^{-7}$), it cannot be dismissed as negligible. This is because we require subradian dephasing throughout the entire inspiral for an accurate extraction of the signal. It is essential to consider even the smallest deviations in order to obtain reliable results. Furthermore, we observe that as time increases, the dephasing $\Delta\phi$ derived for different mass ratios becomes progressively larger.

The expressions of the coordinate-time frequencies ω_r, ω_θ, and ω_ϕ, considering the mass-ratio corrections, are given by [42]

$$\omega_r = \frac{\pi K(k)}{K(k)W + a^2 z_+^2 E[K(k) - E(k)]X}, \tag{10a}$$

$$\omega_\theta = \frac{\pi\beta z_+ X}{2\{K(k)W + a^2 z_+^2 E[K(k) - E(k)]X\}}, \tag{10b}$$

$$\omega_\phi = \frac{K(k)Z + L_z[\Pi(z_-^2, k) - K(k)]X}{K(k)W + a^2 z_+^2 E[K(k) - E(k)]X}. \tag{10c}$$

The expressions of $K(k)$, $E(k)$, $\Pi(z_-^2, k)$, X, z_+, and k are given in Appendix A [Eqs. (A11a)–(A11h)].

In Fig. 3, we show the relative frequency shifts $\Delta\omega/\omega_0 = |\omega_\nu - \omega_0|/\omega_0$ (where the subscript 0 denotes the case of the test particle $\nu = 0$) of four orbits with the same parameters in Fig. 1. We find that the relative frequency shifts increase with the mass ratio. In addition, the relative frequency shifts can be up to about 2 orders ($10^2\nu$) larger than the mass ratio for extremely relativistic orbits.

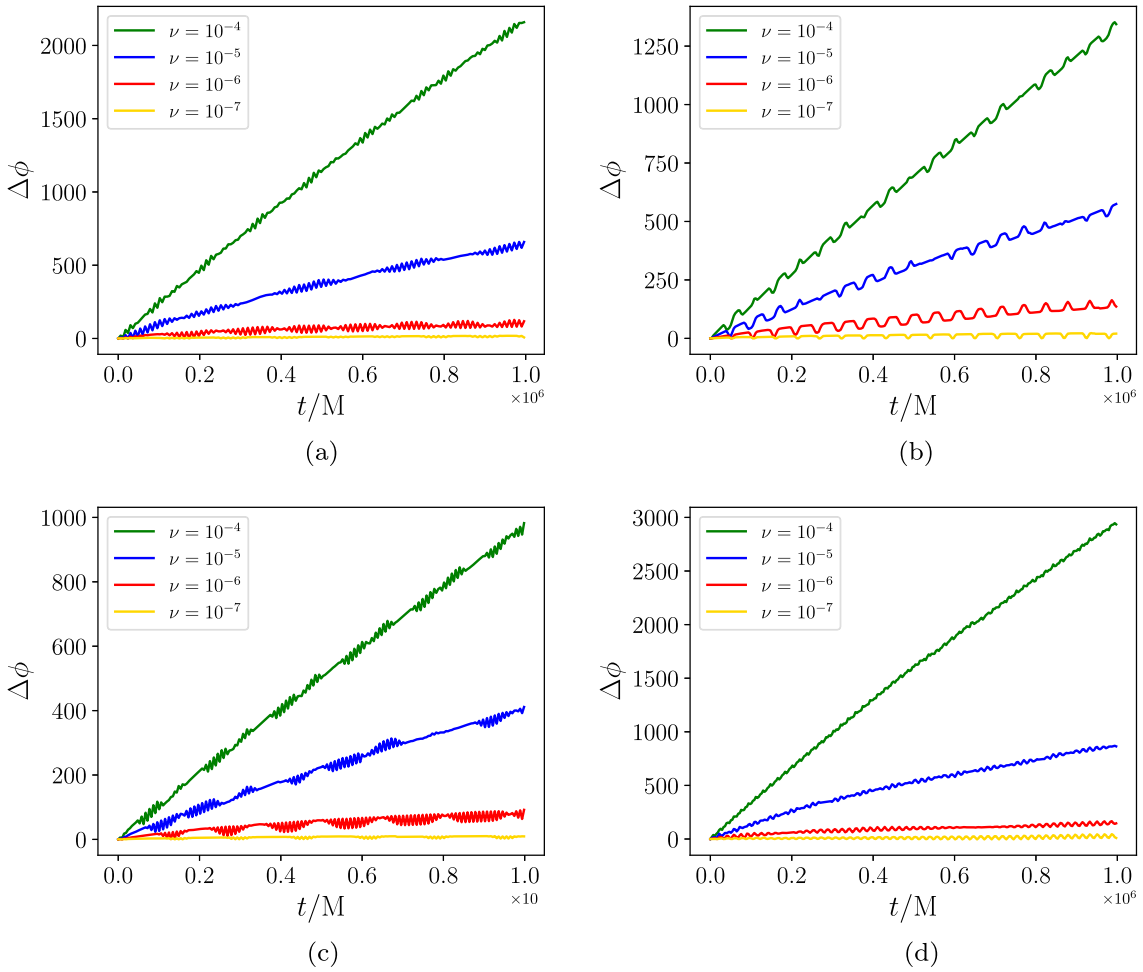

FIG. 2. Dephasing ($\Delta\phi = \phi_\nu - \phi_{\nu=0}$) for different orbital parameters. The green, blue, red, and yellow lines correspond to the cases $\nu = 10^{-4}, 10^{-5}, 10^{-6}$, and $\nu = 10^{-7}$, respectively. (a) $a = 0.99, e = 0.9, \iota = 0°, p = 2.35\mathrm{M}$; (b) $a = 0.95, e = 0.9, \iota = 30°, p = 3.15\mathrm{M}$; (c) $a = 0.9, e = 0.9, \iota = 10°, p = 3.39\mathrm{M}$; (d) $a = 0.98, e = 0.8, \iota = 0°, p = 2.41\mathrm{M}$.

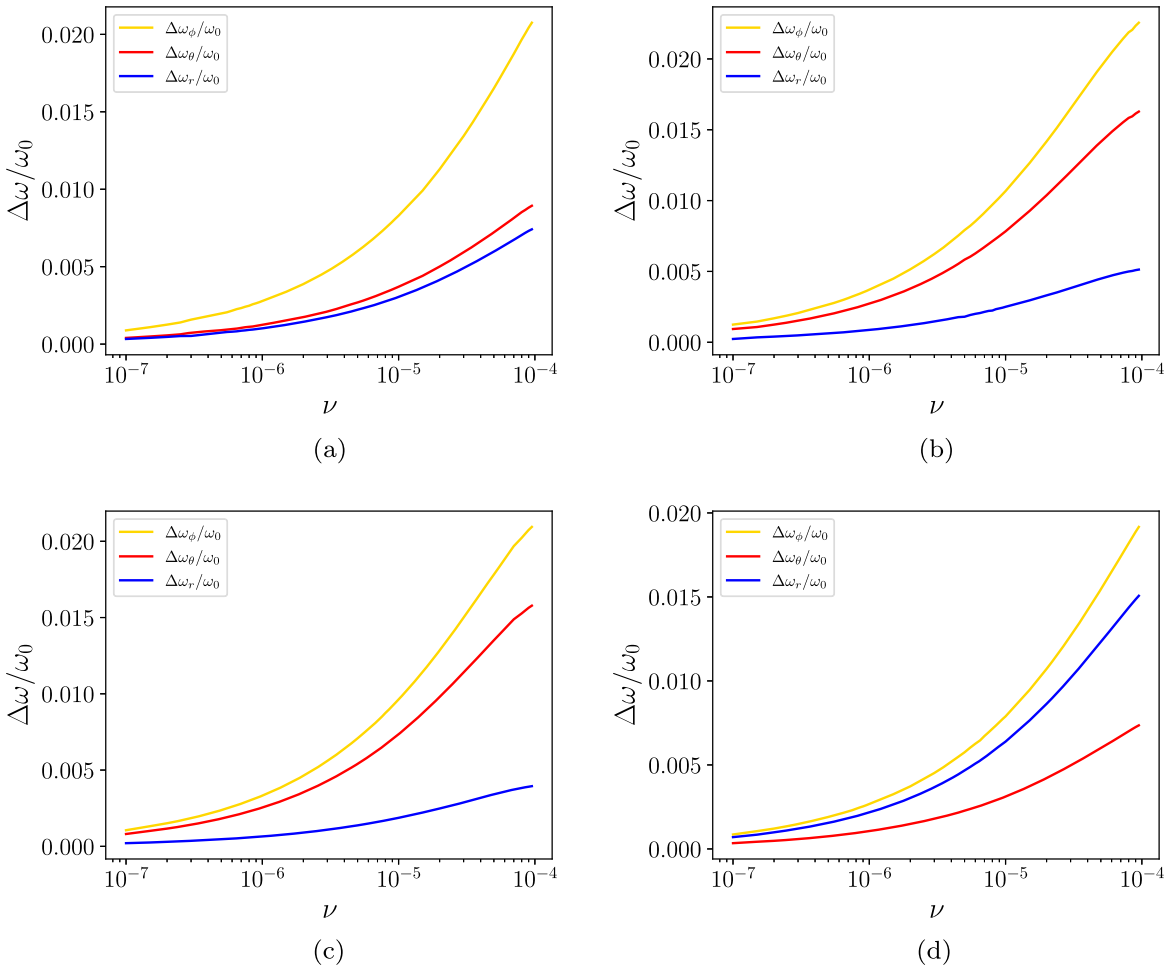

FIG. 3. Frequency shifts $\Delta\omega/\omega_0$ versus mass ratio ν of four orbits with different orbital parameters. The yellow, red, and blue lines represent $\Delta\omega_\phi/\omega_0$, $\Delta\omega_\theta/\omega_0$, and $\Delta\omega_r/\omega_0$, respectively. (a) $a=0.99, e=0.9, \iota=0°, p=2.35$M; (b) $a=0.95, e=0.9, \iota=30°, p=3.15$M; (c) $a=0.9, e=0.9, \iota=10°, p=3.39$M; (d) $a=0.98, e=0.8, \iota=0°, p=2.41$M.

All the above results show that even in the case of extreme mass ratio, the mass-ratio corrections will have a significant impact on orbital frequency, and then affect orbital evolution. This means that when constructing EMRIs' waveform template, the mass ratio should not be ignored. In other words, if we neglect the mass-ratio correction when building EMRIs' waveform template, the final estimated parameters may induce a fake signal of deviation from GR, which will be discussed in more detail in Sec. IV.

We point out that all the results presented in this section only take into account the conservative dynamics, in which the mass-ratio corrections are associated with the conservative part of the 1SF. Though the mass-ratio correction may not correspond to the exact conservative GSF, we can always improve the accuracy of the EOB model by calibrating it with GSF results [21,54,55]. It is important to note that accurately modeling EMRI systems throughout the whole inspiral requires 1PA corrections. Besides the conservative part of 1SF, the dissipative part up to 2SF is also essential and should be taken into account [20,56].

III. WAVEFORMS AND ORBITAL EVOLUTION

The gravitational waveforms can be calculated in the Teukolsky formalism, considering the perturbation on the Weyl scalar ψ_4 [25,57]. At infinity, the GW polarizations $h_{+,\times}$ can be written as

$$\psi_4(r\to\infty)=\frac{1}{2}\frac{\partial^2}{\partial t^2}(h_+ - ih_\times). \tag{11}$$

We decompose ψ_4 in the frequency domain

$$\psi_4=\rho^4\int_{-\infty}^{+\infty}d\omega\sum_{lm}R_{lm\omega}(r)\,{}_{-2}S^{a\omega}_{lm}(\Theta)e^{im\Phi}e^{-i\phi}, \tag{12}$$

where $\rho=-1/(r-ia\cos\theta)$, ω is the discrete frequency spectrum, and $\phi=\int\omega dt$. Here, ${}_{-2}S^{a\omega}_{lm}(\Theta)$ denotes the

spin-weighted ($s=-2$) spherical harmonic coefficient, which depends on the polar angle Θ. The function $R_{lm\omega}(r)$ satisfies the radial Teukolsky equation

$$\Delta^2\frac{d}{dr}\left(\frac{1}{\Delta}\frac{dR_{lm\omega}}{dr}\right)-V(r)R_{lm\omega}=-\mathcal{T}_{lm\omega}(r), \quad (13)$$

where $\Delta=r^2-2Mr+a^2$, $V(r)$ is the potential [Eq. (2.5) of Ref. [58]], and $\mathcal{T}$ is the source term [Eq. (2.14) of Ref. [58]]. The general solution of Eq. (13) is

$$R_{lm\omega}(r)=\frac{R^{\infty}_{lm\omega}(r)}{2i\omega B^{\rm in}_{lm\omega}D^{\infty}_{lm\omega}}\int_{r_+}^{r}dr'\frac{R^{\rm H}_{lm\omega}(r')\mathcal{T}_{lm\omega}(r')}{\Delta(r')^2} +\frac{R^{\rm H}_{lm\omega}(r)}{2i\omega B^{\rm in}_{lm\omega}D^{\infty}_{lm\omega}}\int_{r}^{\infty}dr'\frac{R^{\infty}_{lm\omega}(r')\mathcal{T}_{lm\omega}(r')}{\Delta(r')^2}, \quad (14)$$

where $B^{\rm in}_{lm\omega}$ and $D^{\infty}_{lm\omega}$ are the asymptotic amplitudes [59,60]. $R^{\infty}_{lm\omega}(r)$ and $R^{\rm H}_{lm\omega}(r)$ are the two independent solutions of the homogeneous Teukolsky equation, which are given by

$$R^{\infty}_{lm\omega}(r)=Z^{\rm H}_{lm\omega}r^3e^{i\omega r^*}, \quad (15)$$

$$R^{\rm H}_{lm\omega}(r)=Z^{\infty}_{lm\omega}\Delta^2e^{-ipr^*}, \quad (16)$$

with

$$Z^{\infty}_{lm\omega}=\frac{B^{\rm hole}_{lm\omega}}{2i\omega B^{\rm in}_{lm\omega}D^{\infty}_{lm\omega}}\int_{r}^{\infty}dr'\frac{R^{\infty}_{lm\omega}(r')\mathcal{T}_{lm\omega}(r')}{\Delta(r')^2}, \quad (17)$$

$$Z^{\rm H}_{lm\omega}=\frac{1}{2i\omega B^{\rm in}_{lm\omega}}\int_{r_+}^{r}dr'\frac{R^{\rm H}_{lm\omega}(r')\mathcal{T}_{lm\omega}(r')}{\Delta(r')^2}, \quad (18)$$

where r^* is the tortoise coordinate. The amplitudes $Z^{\rm H,\infty}_{lm\omega}(r)$ fully determine the energy and angular momentum fluxes $\dot{E}^{\rm H,\infty}$, $\dot{L}_z^{\rm H,\infty}$ and the gravitational waveforms

$$\dot{E}^{\infty,\rm H}=\sum_{lm\omega}\frac{|Z^{\rm H,\infty}_{lm\omega}|^2}{4\pi\omega^2}, \quad (19)$$

$$\dot{L}_z^{\infty,\rm H}=\sum_{lm\omega}\frac{m|Z^{\rm H,\infty}_{lm\omega}|^2}{4\pi\omega^3}. \quad (20)$$

Owing to the modification of the orbit by the mass ratio, the orbital averaged energy flux between the EOB orbit and the test particle one could obviously be different. Figure 4 shows that for a mass ratio of 10^{-4}, the energy flux spectrum is visibly different between both cases. Our calculations from the Teukolsky equation show that for the relativistic orbits, the relative difference of the energy fluxes between the EOB and test particle orbits is up to 10ν magnitude. This will produce enough GW dephasing during the long evolution of EMRIs.

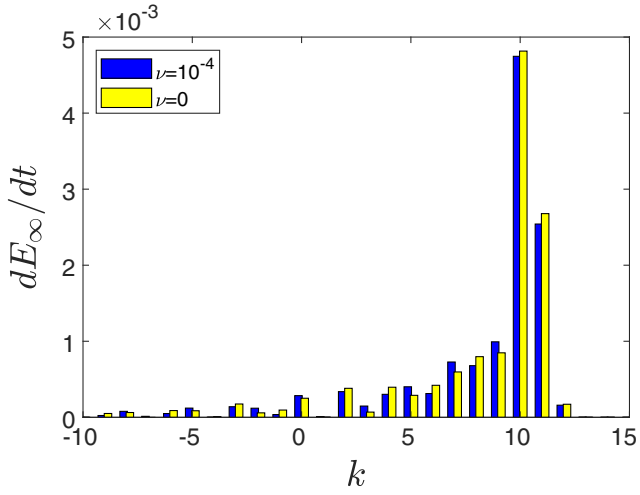

FIG. 4. The spectrum of energy fluxes versus the harmonic number k with parameters $a=0.99$, $p=2.11$, and $e=0.7$. The yellow and blue bar represent $\nu=0$ and $\nu=10^{-4}$, respectively.

For the generic orbits, the particle's motion can be described as the harmonic of the frequency ω_ϕ, ω_θ, and ω_r. We take $\omega=\omega_{mkn}=m\omega_\phi+k\omega_\theta+n\omega_r$, $\phi_{mkn}=\int\omega_{mkn}dt$. Therefore, we can write $h_{+,\times}$ as the multipolar sum of "voices" with these frequencies [61]. For an EMRI system with a total mass M at a distance D, an altitude angle Θ, and an azimuth angle Φ, its GW strain can be written as [30,62]

$$h_+-ih_\times=-\frac{2\mu}{D}\sum_{lmkn}\frac{Z^{\infty}_{lmkn}}{\omega^2_{mkn}}\frac{{}_{-2}S^{a\omega_{mkn}}_{lm}(\Theta)}{\sqrt{2\pi}}e^{-i\phi_{mkn}+im\Phi}, \quad (21)$$

where $\sum_{lmkn}=\sum_{l=2}^{\infty}\sum_{m=-l}^{l}\sum_{k=-\infty}^{\infty}\sum_{n=-\infty}^{\infty}$, and the amplitude Z^{∞}_{lmkn} of each mode can be calculated using the radial Teukolsky equation. Here, ${}_{-2}S^{a\omega_{mkn}}_{lm}(\Theta)$ denotes the spin-weighted ($s=-2$) spherical harmonic coefficient, which depends on the polar angle Θ.

In the present work, we combine the EOB formalism with the Teukolsky equation, i.e., the EOB trajectory sources and the Teukolsky equation, and the latter calculates the waveforms and feeds back the EOB orbit. The gravitational waveforms are generated by using Eq. (21), which is the multipolar sum of "voices" with orbital frequencies ω_ϕ, ω_θ, and ω_r. Since the timescale of gravitational radiation of EMRIs is far larger than the orbital period, we can calculate these frequencies in a short time using Eqs. (10a)–(10c). Unlike the case of the test particle, the EOB dynamics includes the first-order conservative GSF corrections. Note that it may not be entirely exact, but we can always improve the accuracy of the EOB model by calibrating it with GSF results [21,54,55].

Considering the gravitational radiation, the energy, angular momentum, and the Carter constant are no longer conserved. The rates of their changes are expressed by

$$\frac{\mathrm{d}E}{\mathrm{d}t} = \frac{\partial E}{\partial p}\dot{p} + \frac{\partial E}{\partial e}\dot{e} + \frac{\partial E}{\partial \iota}\dot{\iota}, \tag{22a}$$

$$\frac{\mathrm{d}\hat{L}_z}{\mathrm{d}t} = \frac{\partial \hat{L}_z}{\partial p}\dot{p} + \frac{\partial \hat{L}_z}{\partial e}\dot{e} + \frac{\partial \hat{L}_z}{\partial \iota}\dot{\iota}, \tag{22b}$$

$$\frac{\mathrm{d}\hat{Q}}{\mathrm{d}t} = \frac{\partial \hat{Q}}{\partial p}\dot{p} + \frac{\partial \hat{Q}}{\partial e}\dot{e} + \frac{\partial \hat{Q}}{\partial \iota}\dot{\iota}. \tag{22c}$$

By solving Eqs. (22a)–(22c), we can describe the evolution of orbital parameters (p, e, ι) by

$$\dot{p} = c_{(\hat{L}_z,\hat{Q})(e,\iota)}\frac{\mathrm{d}E}{\mathrm{d}t} + c_{(E,\hat{Q})(\iota,e)}\frac{\mathrm{d}\hat{L}_z}{\mathrm{d}t} + c_{(E,\hat{L}_z)(e,\iota)}\frac{\mathrm{d}\hat{Q}}{\mathrm{d}t}, \tag{23a}$$

$$\dot{e} = c_{(\hat{L}_z,\hat{Q})(\iota,p)}\frac{\mathrm{d}E}{\mathrm{d}t} + c_{(E,\hat{Q})(p,\iota)}\frac{\mathrm{d}\hat{L}_z}{\mathrm{d}t} + c_{(E,\hat{L}_z)(\iota,p)}\frac{\mathrm{d}\hat{Q}}{\mathrm{d}t}, \tag{23b}$$

$$\dot{\iota} = c_{(\hat{L}_z,\hat{Q})(p,e)}\frac{\mathrm{d}E}{\mathrm{d}t} + c_{(E,\hat{Q})(e,p)}\frac{\mathrm{d}\hat{L}_z}{\mathrm{d}t} + c_{(E,\hat{L}_z)(p,e)}\frac{\mathrm{d}\hat{Q}}{\mathrm{d}t}, \tag{23c}$$

where the coefficients are given by

$$c_{(C_1,C_2)(o_1,o_2)} = \frac{\frac{\partial C_1}{\partial o_1}\frac{\partial C_2}{\partial o_2} - \frac{\partial C_1}{\partial o_2}\frac{\partial C_2}{\partial o_1}}{\left[\frac{\partial E}{\partial \iota}\frac{\partial \hat{L}_z}{\partial p} - \frac{\partial E}{\partial p}\frac{\partial \hat{L}_z}{\partial \iota}\right]\frac{\partial \hat{Q}}{\partial e} + \left[\frac{\partial E}{\partial e}\frac{\partial \hat{L}_z}{\partial \iota} - \frac{\partial E}{\partial \iota}\frac{\partial \hat{L}_z}{\partial e}\right]\frac{\partial \hat{Q}}{\partial p} + \left[\frac{\partial E}{\partial p}\frac{\partial \hat{L}_z}{\partial e} - \frac{\partial E}{\partial e}\frac{\partial \hat{L}_z}{\partial p}\right]\frac{\partial \hat{Q}}{\partial \iota}}. \tag{24}$$

Once we have the GW fluxes $\dot{E}$, $\dot{L}_z$, and $\dot{Q}$, substituting expressions of these fluxes into Eqs. (23a)–(23c), we can derive the orbital evolution. The ${}_{-2}S_{lm}^{a\omega_{mkn}}$ and Z_{lmkn}^{∞} can be computed by using the analytical module of the Black Hole Perturbation Club code [63–65]. Combining Eqs. (10a)–(10c) and (21), we can generate the gravitational waveforms. However, fully using the numerical Teukolsky-based fluxes is computationally expensive. Without impacting our main target, we here employ a hybrid scheme of fluxes [44].

Compared with the numerical fluxes, the GG formalism performs well for orbits of low eccentricity, especially for circular, inclined orbits. We also include mass-ratio corrections (dissipative 1PA term) to the original second post-Newtonian (2PN) fluxes based on [43,65,66], though this has almost no influence on the data analysis results. The final expressions for $\dot{E}$, $\dot{L}_z$, and $\dot{Q}$ [Eqs. (B1)–(B3) with Eqs. (B7)–(B8) and Eqs. (B10)–(B12)] are given in Appendix B.

As an example, Fig. 5 shows two waveforms including or excluding mass-ratio corrections starting at $(p_0, e_0, \iota_0) = (6.84, 0.166, 45°)$, and the mass ratio is 10^{-5}. We plot the one-year evolving waveforms at the viewing angle $(\Theta, \Phi) = (45°, 0°)$. In our work, we generate the

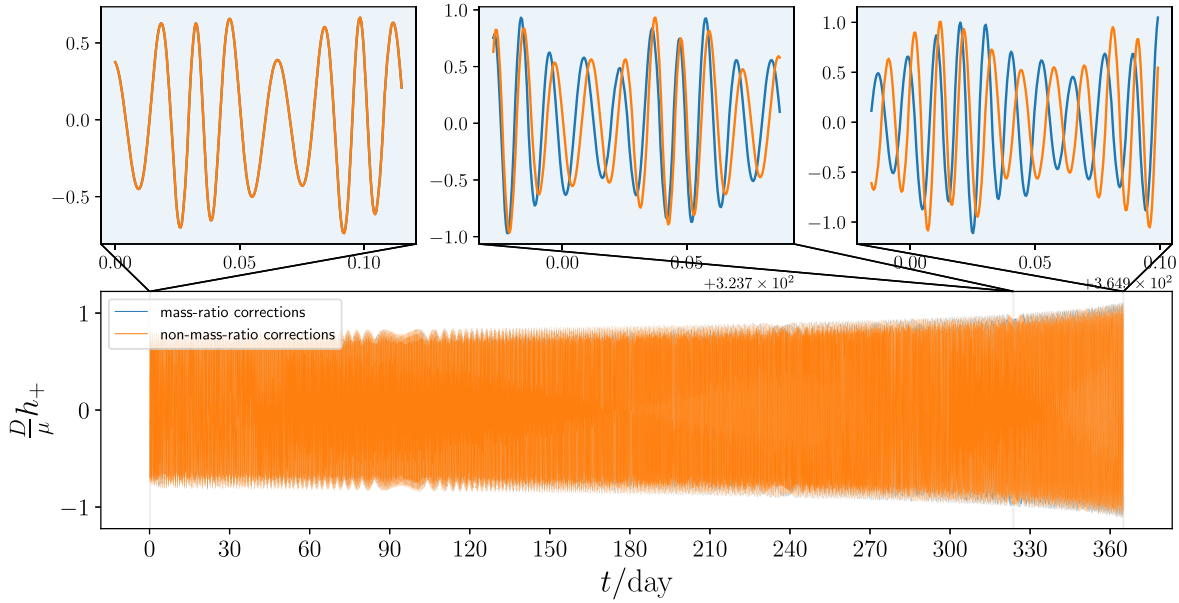

FIG. 5. Two waveforms of EMRI systems with $(M, \mu, a) = (5 \times 10^6 M_\odot, 50 M_\odot, 0.43)$, starting at $(p_0, e_0, \iota_0) = (6.84, 0.166, 45°)$. We plot the one-year evolving waveform at the viewing angle $(\Theta, \Phi) = (45°, 0°)$. The orange line represents the waveform excluding mass-ratio corrections, and the blue line denotes the waveform including mass-ratio corrections. The waveforms are generated using the Black Hole Perturbation Club's Teukolsky code [63,64].

gravitational waveforms only considering the $(l,m) = (2,2)$ mode, which is the dominant strain mode. The bottom row and the top one represent the one-year evolving waveforms and their three enlarged waveforms, respectively. From magnified waveforms (top row), we can see that at the beginning (left column), the difference between two gravitational waveforms with or without mass-ratio corrections is quite small, which is invisible to the naked eye. However, waveform errors due to the mass ratio can accumulate as time goes by. And then obvious waveform differences (both in dephasing and amplitude) can be found in the waveforms at the latter stage of evolution (middle and right columns).

The accumulative errors are caused by the dual effects of mass-ratio correction on the orbital frequencies and the Teukolsky-based energy fluxes. First of all, under the same orbital parameters, mass ratio will affect the orbital frequencies and thus impact the frequencies of GWs at $O(\nu) - O(10^2\nu)$ depending on the orbital parameters. Furthermore, the orbit correction caused by mass ratio will change the Teukolsky-based energy fluxes with a relative difference above $O(\nu)$ for relativistic trajectory. Under the joint influence of these two factors, when the mass-ratio correction is not considered in the orbit dynamics, i.e., calculate the geodesic in the background field of the massive body and then evolve the orbit by the adiabatic approximation (the radiation reaction is considered as the leading order self-force), it may produce accumulative errors that cannot be ignored for EMRI waveforms.

IV. DATA ANALYSIS AND RESULTS

The matched filtering [67] technique is widely used in LIGO and Virgo data processing, and it will also be applicable to future space-borne GW detectors. We also apply this technique to analyze the influence of mass-ratio corrections on EMRI waveforms quantitatively. Given two time series $a(t)$ and $b(t)$, their maximized fitting factor (overlap) and mismatch ($\mathcal{M}$) are given by

$$\text{overlap} = \max_{t_s,\phi_s} \frac{(a(t)|b(t+t_s)e^{i\phi_s})}{\sqrt{(a|a)(b|b)}}, \tag{25}$$

$$\mathcal{M} = 1 - \text{overlap} = 1 - \max_{t_s,\phi_s} \frac{(a(t)|b(t+t_s)e^{i\phi_s})}{\sqrt{(a|a)(b|b)}}, \tag{26}$$

where t_s is the time shift, ϕ_s is the phase shift, and $(a|b)$ is the inner product between two time series signals $a(t)$ and $b(t)$ with the following expression:

$$(a|b) = 2\int_0^\infty df \frac{\tilde{a}^*(f)\tilde{b}(f) + \tilde{a}(f)\tilde{b}^*(f)}{S_n(f)}, \tag{27}$$

where $\tilde{a}(f)$ is the Fourier transform of the series signal $a(t)$, $\tilde{a}^*(f)$ is the complex conjugate of $\tilde{a}(f)$, and $S_n(f)$ is the power spectral density (PSD). In this work, we use the PSD from the Online Sensitivity Curve Generator website [68,69], representative of the design sensitivity of LISA.

We use the PyCBC library [70] to compute the mismatch between two EMRI waveforms at a distance of 1 Gpc, and the result is presented in Fig. 6. We fix the mass of the SCO at $50M_\odot$ and consider four EMRI systems with mass ratios ranging from 10^{-4} to 10^{-7}. The results show that when the mass ratio ($\nu = 10^{-6}$ and $\nu = 10^{-7}$) is closer to the test particle limit ($\nu = 0$), the mismatch is so small that it can be ignored. In addition, for the case of $\nu = 10^{-4}$ and $\nu = 10^{-5}$, as time passes, the mismatches between two waveforms will increase and may be large enough to induce a fake signal of deviation from GR, which will be explained later.

We follow the method of Moore [40] *et al.* to calculate fake Bayesian factors for the deviation from GR. First, it is assumed that GR is the correct description of nature. For the combined parameter space $\lambda = (\alpha;\theta)$, the observed signal, s, can be described as the sum of the GW signal and the detector noise:

$$s = n + h(\alpha;\theta) = n + h(\alpha_{\rm Tr} = 0;\theta_{\rm Tr}) + \Delta h(\theta_{\rm Tr}). \tag{28}$$

Here, we treat α as the modified gravity parameter, and in the case of GR, α is equal to 0. θ denotes the source parameters including both intrinsic (masses, spins, etc.) and extrinsic (distance, viewing angles, etc.) parameters. $\Delta h(\theta_{\rm Tr})$ represents the errors caused by inaccurate waveform templates.

Assuming the instrument noise is Gaussian, the likelihood $\mathcal{L}(\alpha;\theta) = P(s|\alpha;\theta)$ is

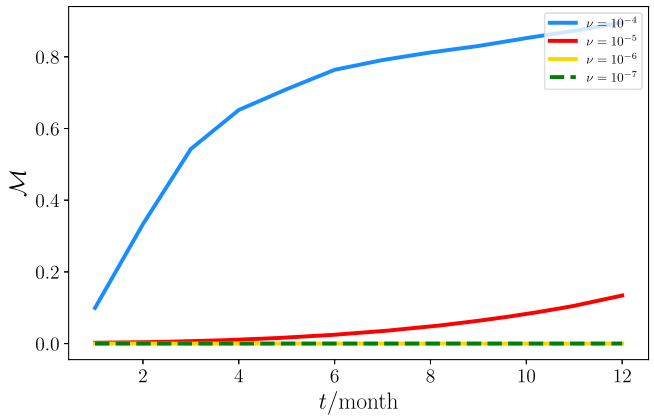

FIG. 6. The mismatches of waveforms coming from EOB dynamical evolutions and the test particle one. The blue, red, yellow, and green lines represent systems with different mass ratios of 10^{-4}, 10^{-5}, 10^{-6}, and 10^{-7}, respectively. For each ν, we calculate the mismatch considering different evolution times from 1 month to 12 months. We fix the EMRI parameters to $a = 0.9$, $(\mu, M) = (50M_\odot, \mu/\nu)$ at the distance of 1 Gpc. Our waveforms end at $(p, e, \iota) = (5.1, 0.1, 80°)$.

$$\log \mathcal{L}(\alpha;\theta) = -\frac{1}{2}|s - h(\alpha;\theta)|^2 + c = -\frac{1}{2}|n - \delta h(\alpha;\theta) + \Delta h(\theta_{\rm Tr})|^2 + c, \quad (29)$$

where we set $\delta h(\alpha;\theta) = h(\alpha;\theta) - h(\alpha_{\rm Tr};\theta_{\rm Tr})$ and c is a constant. For simplicity, we assume that the prior on λ is flat, so the posterior is proportional to the likelihood. The maximum likelihood (ML) parameters can be decomposed into the following three parts

$$\lambda_{\rm ML} = \lambda_{\rm Tr} + \Delta\lambda_{\rm stat} + \Delta\lambda_{\rm sys}, \quad (30)$$

where $\lambda_{\rm Tr}$ is the true source parameters; $\Delta\lambda_{\rm stat}$ is the statistical error, which depends on the instrument noise n; and $\Delta\lambda_{\rm sys}$ is the systematic error, which depends on the model error Δh. Through the first-order Taylor expansion of Δh, the log-likelihood at the ML parameters is given by [40]

$$\log \mathcal{L}(\lambda) = c' - \frac{1}{2}\Gamma_{\mu\nu}(\lambda - \lambda_{\rm ML})^{\mu}(\lambda - \lambda_{\rm ML})^{\nu}, \quad (31)$$

where c' is another constant, $\Gamma_{\mu\nu}$ is the Fisher matrix, and we assume that $\Gamma_{oi} = 0$ if $i \neq 0$. We set $k = \dim(\theta)$, that is, $\dim(\lambda) = k + 1$. For the non-GR submodel, The Bayesian evidence integral is given by

$$Z_{\rm non-GR} = \int d\lambda \mathcal{L}(\lambda) = e^{c'}\sqrt{\frac{(2\pi)^{k+1}}{\det\Gamma_{\mu\nu}}}. \quad (32)$$

For the GR submodel, $\alpha = 0$, we have

$$\log \mathcal{L}_{\rm GR}(\theta) = c' - \frac{1}{2}\Gamma_{00}\alpha_{\rm ML}^2 - \frac{1}{2}(\theta - \theta_{\rm ML})^i\Gamma_{ij}(\theta - \theta_{\rm ML})^j, \quad (33)$$

$$Z_{\rm GR} = \int d\theta \mathcal{L}_{\rm GR}(\theta) = e^{c' - \Gamma_{00}\alpha_{\rm ML}^2/2}\sqrt{\frac{(2\pi)^k}{\det\Gamma_{ij}}}, \quad (34)$$

with

$$\alpha_{\rm ML} = \alpha_{\rm stat} + \alpha_{\rm sys}, \quad (35a)$$

$$\alpha_{\rm stat} = \frac{z}{\rho}, \quad (35b)$$

$$\alpha_{\rm sys} = \sqrt{2\mathcal{M}}\cos\iota, \quad (35c)$$

$$\sigma_{\alpha} = \frac{1}{\rho}, \quad (35d)$$

$$\Gamma_{00} = \sigma_{\alpha}^{-2}, \quad (35e)$$

where $z \sim N(0,1)$ is the random number associated with the noise realization, ρ is the SNR of the signal, $\mathcal{M}$ is the mismatch given in Eq. (26), σ_{α} is the standard deviation of the distribution, and ι is the angle between the signals $\Delta h(\theta_{\rm Tr})$ and $\partial h/\partial\alpha$. The Bayes factor in favor of the deviation from GR is

$$\mathcal{B} = \frac{\Pi}{A}\frac{Z_{\rm non-GR}}{Z_{\rm GR}}, \quad (36)$$

where Π is the prior Bayes factor and $A = \alpha_{\rm max} - \alpha_{\rm min}$ is the prior range of α. With the assumption that $\Gamma_{0i} = 0$, $\det\Gamma_{\mu\nu} = \Gamma_{00}\det\Gamma_{ij}$, the Bayes factor simplifies to

$$\mathcal{B} = \frac{\Pi}{A}\sqrt{\frac{2\pi}{\Gamma_{00}}}\exp\left(\frac{1}{2}\Gamma_{00}\alpha_{\rm ML}^2\right). \quad (37)$$

Inserting the expressions in Eqs. (35a)–(35e) into Eq. (37), the logarithm of the Bayes factor is given by

$$\log\mathcal{B} = \log\left(\frac{\Pi}{A}\frac{\sqrt{2\pi}}{\rho}\right) + \frac{(z + \rho\sqrt{2\mathcal{M}}\cos\iota)^2}{2}. \quad (38)$$

In this work, our results are scaled to $\Pi = A = 1$, $z = 0$, $\cos\iota \to \cos\iota_m = 1$, and the threshold of the Bayes factor $\mathcal{B}_{\rm threshold} = e^{10}$ as in Ref. [40]. The final expression of $\log\mathcal{B}$ is

$$\log\mathcal{B} = \log\left(\frac{\sqrt{2\pi}}{\rho}\right) + \mathcal{M}\rho^2. \quad (39)$$

Fig. 7 shows the logarithm of the Bayes factor as a function of SNR and mismatch ($\mathcal{M}$). We take the mismatches ranging from 10^{-2} to 0.5 and SNRs ranging from 5 to 30. The yellow line represents the threshold (10) of $\log\mathcal{B}$, above which we may mistakenly claim to have

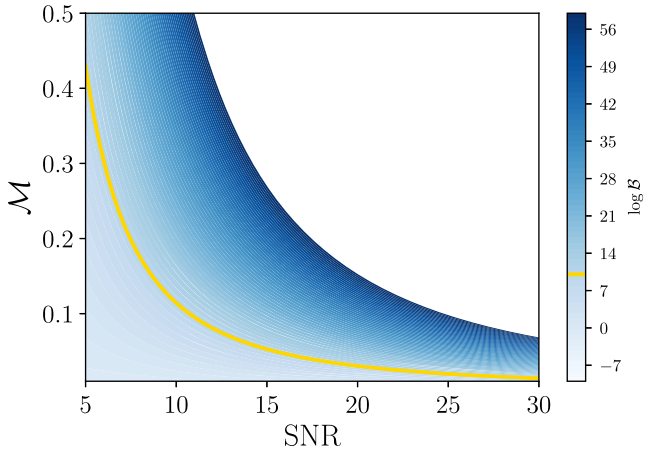

FIG. 7. The logarithm of the Bayes factor, $\log\mathcal{B}$, of the EMRI systems with different SNR and mismatch ($\mathcal{M}$) values. The yellow line represents the threshold (10) of $\log\mathcal{B}$.

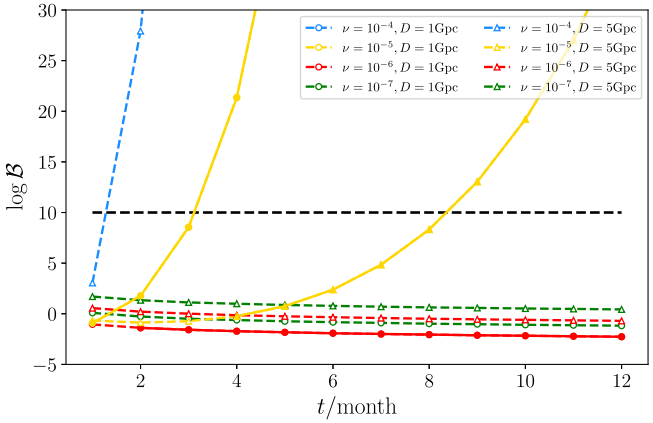

FIG. 8. The logarithm of the Bayes factor ($\log \mathcal{B}$) versus evolution times for the EMRI systems with the same orbital parameters in Fig. 6. The dashed blue, yellow, red, and green lines represent systems with different mass ratios of 10^{-4}, 10^{-5}, 10^{-6}, and 10^{-7}, respectively. The dashed black line denotes the threshold (10) of $\log \mathcal{B}$. The circles and the triangles mark EMRIs at the distance of 1 Gpc and 5 Gpc, respectively. Solid triangles or circles connected by solid lines indicate EMRI systems with detectable SNRs greater than 10.

detected a deviation from GR. We can see that even if the mismatch ($\mathcal{M}$) is small, the calculated $\log \mathcal{B}$ may still exceed the threshold when the SNR is very large, which may induce a fake signal of deviation from GR.

As we described in Fig. 6, the mismatch of waveforms is related to the duration of signals. With the accumulation of time, the mismatch between the two signals will increase. In addition, the SNR depends on both the luminosity distance of the source and the signal length. As an example, Fig. 8 shows the logarithm of the Bayes factor for different luminosity distances. We choose the same orbital parameters as in Fig. 6. Solid triangles or circles connected by solid lines indicate EMRI systems with detectable SNRs greater than 10. Our results show that for the system with a mass ratio of $\nu = 10^{-4}$, the calculated Bayesian factor will still exceed the threshold (10) even when it is far away from us (5 Gpc) due to its high mismatch and SNR, which may lead to a misjudgment of testing GR. For the case of $\nu = 10^{-5}$, the source at 1 Gpc can also lead to the same misjudgment. However, for the system with a mass ratio of $\nu = 10^{-6\sim-7}$, due to its small mismatch, even if the SNR reaches a detectable threshold, it will not induce a false signal that deviates from GR predictions.

In Table I, for quantitative comparison, we list the logarithm of the Bayes factor ($\log \mathcal{B}$) due to mass ratio for twenty different systems. We find that in the case of $\nu \gtrsim 10^{-5}$, when the SNR is high enough, ignoring the mass ratio may indicate a deviation from the GR. However, for the EMRI system with a smaller mass ratio, there is almost no possibility that we will make a wrong judgment.

TABLE I. The logarithm of the Bayes factors ($\log \mathcal{B}$) between two waveforms including or excluding mass-ratio corrections. The signals continue for one year and end at $(e_{\rm fin}, \iota_{\rm fin}, p_{\rm fin})$.

N	a	$e_{\rm fin}$	$\iota_{\rm fin}(^\circ)$	$p_{\rm fin}$ (M)	μ ($M_\odot$)	ν	D (Gpc)	$\mathcal{M}$	SNR	$\log \mathcal{B}$
1	0.30	0.12	45	5.7	50	1×10^{-4}	2.5	8.4×10^{-1}	150.1	18921.1
2	0.43	0.10	72	7.2	20	6×10^{-5}	1.5	4.7×10^{-1}	78.4	2885.4
3	0.73	0.08	81	5.8	25	6×10^{-5}	7.0	7.4×10^{-1}	16.2	192.3
4	0.14	0.16	70	6.9	35	5×10^{-5}	2.0	3.0×10^{-1}	81.8	2003.9
5	0.80	0.15	60	6.5	40	4×10^{-5}	6.0	4.0×10^{-1}	35.8	510.0
6	0.35	0.13	35	6.4	30	4×10^{-5}	5.0	1.9×10^{-1}	51.8	506.8
7	0.60	0.10	45	5.2	25	3×10^{-5}	3.0	5.6×10^{-1}	62.6	2191.3
8	0.70	0.20	10	6.0	20	3×10^{-5}	2.0	4.4×10^{-1}	80.7	2862.0
9	0.80	0.10	70	5.2	40	2×10^{-5}	1.0	3.4×10^{-1}	134.4	6137.6
10	0.90	0.20	85	6.3	45	1×10^{-5}	8.0	2.4×10^{-2}	9.0	0.7
11	0.70	0.12	50	6.0	35	1×10^{-5}	1.5	1.6×10^{-2}	78.5	95.2
12	0.10	0.30	40	7.1	30	8×10^{-6}	3.0	2.4×10^{-3}	38.5	0.8
13	0.60	0.22	45	7.2	40	6×10^{-6}	4.5	2.4×10^{-4}	24.6	−2.1
14	0.55	0.40	38	6.8	30	5×10^{-6}	1.0	1.2×10^{-3}	87.9	5.7
15	0.85	0.15	30	5.5	50	4×10^{-6}	2.0	1.1×10^{-3}	48.7	−0.4
16	0.20	0.35	55	7.0	30	3×10^{-6}	8.0	2.5×10^{-4}	7.1	−1.0
17	0.40	0.30	50	6.5	25	2×10^{-6}	5.0	1.3×10^{-4}	8.8	−1.2
18	0.50	0.22	20	6.0	10	2×10^{-6}	4.0	5.0×10^{-4}	8.9	−1.2
19	0.30	0.40	35	6.8	25	1×10^{-6}	1.0	1.9×10^{-5}	58.8	−3.1
20	0.62	0.30	60	5.8	10	1×10^{-6}	3.5	6.2×10^{-4}	4.9	−0.7

V. CONCLUSIONS

In this work, based on the EOB orbits and Teukolsky equation, we investigated the influence of mass-ratio corrections on the orbital motion (orbit, frequency, and phase) and gravitational radiation. Our results show that even in the case of extreme mass ratio, the mass-ratio corrections may have a great impact on orbital frequency, and then affect orbital evolution. In addition, we also illustrated the discrepancy in Teukolsky-based energy fluxes caused by mass ratio, in which case the gravitational radiation was considered. We find that for the relativistic orbits, the relative difference of energy fluxes between the EOB orbit and the test particle one is about 10ν in magnitude, which cannot be ignored. Both the difference in conservation dynamics and that in Teukolsky-based energy fluxes may generate accumulated errors during the long-term evolution of EMRIs and then affect the waveforms. This means that when constructing waveform templates of EMRIs, the mass ratio cannot be ignored in the orbital calculation. In other words, if we neglect the mass-ratio corrections when building the EMRI waveform templates, there is a risk of inducing a fake signal of deviation from GR.

One of the scientific goals of the study of EMRIs is to test GR and the nature of BHs. In order to support this goal, an accurate and effective waveform template is needed. However, this is still a challenge at present. The waveform template given in this work, combining EOB orbits and the Teukolsky equation, including mass-ratio corrections, is more accurate than the test particle one. Based on the Bayesian analysis, we evaluated the possibility of inducing a fake signal of deviation from GR because of the omission of the mass-ratio corrections in waveform templates. We find that for the case of $\nu \lesssim 10^{-5}$, the mismatch of waveforms coming from EOB dynamical evolutions and the test particle one is so small that it can be ignored. However, for the case of $\nu \gtrsim 10^{-5}$, the mismatch is much bigger, and there is a risk of making an incorrect judgment, namely, that we have detected a deviation from GR. We may conclude that the mass-ratio correction in the EMRI waveform templates is important, especially when $\nu \gtrsim 10^{-5}$.

It is noted that we just use EOB dynamics to include the conservative mass-ratio correction which may not exactly describe the self-force effect at the extreme mass-ratio limit. However, our result should be kept at least qualitatively correct. We will compare our findings with existing waveforms such as those obtained from the GSF formalism [21] or the numerical relativity simulations to validate our results and assess agreement between different approaches in the future. In our current study, we have not considered the spin of the secondary and its potential impact on the metric of the central black hole. However, in future work, we plan to investigate the effects of the spin of the smaller object and estimate the order of magnitude of the spin contributions in our analyses [56,71,72]. Doing so could provide a more accurate picture of the dynamics of compact object inspirals in such extreme gravitational environments.

In our Bayesian parameter inference, we used a simple linearized analysis with the help of Fisher matrix calculation. We use a Gaussian distribution as a prior to describe the detector noise. It is known that this is not the case, due to a lot of transient noise that affects the sensitivity of the detector, so a more suitable prior could be used to improve our work. We should point out that GR is assumed to be the correct description of nature in this work, which is not necessarily correct. If instead we use gravitational waveforms for data analysis but GR is wrong (stealth bias) [73], what will happen to the results? A joint analysis will be conducted by using the waveforms with the GR assumption in the present paper and the non-GR one to confirm whether ignoring the mass ratio in waveform templates will induce misjudgment on testing GR in the forthcoming work. In addition, here we only discussed the fake deviation of GR caused due to the omission of the mass ratio for a single GW event. However, waveform errors may accumulate as the catalog size increases and lead to incorrect scientific conclusions [40,41]. In the future, we will also study the case of GW events in the catalog using a hierarchical Bayesian approach with the assumption that the non-GR parameters follow Gaussian distribution [74]. We hope our work will be useful for developing EMRI waveform templates for space-borne GW detectors.

ACKNOWLEDGMENTS

This work was supported by the National Key R&D Program of China (Grant No. 2021YFC2203002) and the National Natural Science Foundation of China (Grant No. 12173071). Wen-Biao Han was supported by the CAS Project for Young Scientists in Basic Research (Grant No. YSBR-006). This work made use of the High Performance Computing Resource in the Core Facility for Advanced Research Computing at Shanghai Astronomical Observatory. We also thank Belahcene Imene for her valuable advice on this work.

APPENDIX A: EOB FORMALISM

The metric potentials A and D for the EOB formalism mentioned in Ref. [51] are given by

$$A(u) = \Delta_u - \frac{a^2}{M^2}u^2 \tag{A1a}$$

$$D^{-1}(U) = 1 + \log(D_{\text{Taylor}}) \tag{A1b}$$

with

$$\Delta_u = \bar{\Delta}_u(\Delta_0\nu + \nu\log(\Delta_5 u^5 + \Delta_4 u^4 + \Delta_3 u^3 + \Delta_2 u^2 + \Delta_1 u + 1) + 1) \tag{A2a}$$

$$\bar{\Delta}_u = \frac{a^2u^2}{M^2} + \frac{1}{(K\nu-1)^2} + \frac{2u}{K\nu-1} \tag{A2b}$$

$$\Delta_5 = (K\nu-1)^2\left[\frac{64}{5}\log(u) + \left(-\frac{1}{3}a^2(\Delta_1^3 - 3\Delta_1\Delta_2 + 3\Delta_3) - \frac{\Delta_1^5 - 5\Delta_1^3\Delta_2 + 5\Delta_1^2\Delta_3 + 5\Delta_1\Delta_2^2 - 5\Delta_2\Delta_3 - 5\Delta_4\Delta_1}{5(K\nu-1)^2} + \frac{\Delta_1^4 - 4\Delta_1^2\Delta_2 + 4\Delta_1\Delta_3 + 2\Delta_2^2 - 4\Delta_4}{2(K\nu-1)} + \frac{2275\pi^2}{512} + \frac{128\gamma}{5} - \frac{4237}{60} + \frac{256\log(2)}{5}\right]\right. \tag{A2c}$$

$$\Delta_4 = \frac{1}{96}[8(6a^2(\Delta_1^2 - 2\Delta_2)(K\nu-1)^2 + 3\Delta_1^4 + \Delta_1^3(8 - 8K\nu) - 12\Delta_1^2\Delta_2 + 12\Delta_1(2\Delta_2 K\nu - 2\Delta_2 + \Delta_3) + 48\Delta_2^2 - 64(K\nu-1)(3\Delta_3 - 47K\nu + 47) - 123\pi^2(K\nu-1)^2] \tag{A2d}$$

$$\Delta_3 = -a^2\Delta_1(K\nu-1)^2 - \frac{\Delta_1^3}{3} + \Delta_1^2(K\nu-1) + \Delta_1\Delta_2 - 2(K\nu-1)(\Delta_2 - K\nu + 1) \tag{A2e}$$

$$\Delta_2 = \frac{1}{2}(\Delta_1(\Delta_1 - 4K\nu + 4) - 2a^2\Delta_0(K\nu-1)^2) \tag{A2f}$$

$$\Delta_1 = -2(\Delta_0 + K)(K\nu-1) \tag{A2g}$$

$$\Delta_0 = K(K\nu-2) \tag{A2h}$$

$$D_{\text{Taylor}} = 1 + 6\nu u^2 + 2\nu u^3(26 - 3\nu). \tag{A2i}$$

The Hamilton-Jacobi equation is given by [45]

$$g^{\alpha\beta}P_\alpha P_\beta + \frac{Q_4 M^2 P_r^4}{r^2\mu^2} + \mu^2 = 0, \tag{A3}$$

where the nongeodesic term $Q_4 = \frac{2(4-3\nu)\nu M^2}{r^2}$ appears at 3PN order, and here we omit this term as in Ref. [42]. $P_t = -H_{\text{eff}}$, $P_\phi = L_z$. By substituting the metric expressions (6) into Eq. (A3), we get four conserved quantities of motion,

$$\hat{Q} = \cos^2\theta_{\min}\left[a^2(1 - \hat{H}_{\text{eff}}^2) + \frac{\hat{L}_z^2}{\sin^2\theta_{\min}}\right] \tag{A4}$$

$$H_{\text{eff}} = \frac{g^{t\phi}}{g^{tt}}P_\phi + \frac{1}{\sqrt{-g^{tt}}}\sqrt{\mu^2 + \left[g^{\phi\phi} - \frac{(g^{t\phi})^2}{g^{tt}}\right]P_\phi{}^2 + g^{rr}P_r^2 + g^{\theta\theta}P_\theta^2} \tag{A5}$$

$$\hat{L}_z^2 = \frac{(a_1-a_2)^2(b_1+b_2)^2 - (b_1^2-b_2^2)(b_1^2c_1 - b_2^2c_2) - 2(a_1-a_2)b_1b_2\sqrt{(a_1-a_2)^2 - (b_1^2-b_2^2)(c_1-c_2)}}{[(a_1-a_2)^2 - (b_1^2c_1 - b_2^2c_2)]^2} \tag{A6}$$

$$\frac{E^2}{M^2} = 1 + 2\nu\left(a_1\hat{L}_z + \sqrt{\frac{c_1\hat{L}_z^2 + 1}{b_1}} - 1\right) \tag{A7}$$

with

$$a_1 = \frac{\tilde{\omega}_{\text{fd1}}}{\Lambda_{t1}} \tag{A8a}$$

$$a_2 = \frac{\tilde{\omega}_{\text{fd2}}}{\Lambda_{t2}} \tag{A8b}$$

$$b_1 = \sqrt{\frac{\Sigma_1\Delta_{t1}}{\Lambda_{t1}}} \tag{A8c}$$

$$b_2 = \sqrt{\frac{\Sigma_2\Delta_{t2}}{\Lambda_{t2}}} \tag{A8d}$$

$$c_1 = \frac{\Sigma_1}{(1 - \cos^2\theta_{\min})\Lambda_{t1}} \tag{A8e}$$

$$c_2 = \frac{\Sigma_2}{(1 - \cos^2\theta_{\min})\Lambda_{t2}}. \tag{A8f}$$

With the help of these constants of motion, we can drive the expressions of angular momentum by

$$\hat{P}_\theta{}^2 = \hat{Q} - \cos^2\theta_{\min}\left[a^2(1-\hat{H}_{\rm eff}^2) + \frac{\hat{L}_z^2}{\sin^2\theta_{\min}}\right] \tag{A9a}$$

$$\hat{P}_r{}^2 = \frac{[a\hat{L}_z - (r^2+a^2)H_{\rm eff}^2]^2 - (r^2A(u)+a^2)\left[r^2 + \hat{k} + 2\frac{\tilde{\omega}_{\rm fd}^2 + ar^2(A(u)-1)}{r^2A(u)+a^2}\hat{H}_{\rm eff}\hat{L}_z - G(r)\hat{L}_z^2\right]}{(r^2A(u)+a^2)^2D^{-1}(u)} \tag{A9b}$$

$$P_\phi = L_z, \tag{A9c}$$

where P_θ, P_r, and P_ϕ are the polar, radial, and azimuthal angular momentum.

From Eqs. (6), (A4)–(A7), and (A9), the orbital evolution equations for r, ϕ, and θ can be obtained by

$$\dot{r} = \frac{\partial E}{\partial P_r} = -\frac{g^{rr}\hat{P}_r}{E/M(g^{tt}\hat{H}_{\rm eff} - g^{t\phi}\hat{L}_z)} \tag{A10a}$$

$$\dot{\phi} = \frac{\partial E}{\partial P_\phi} = \frac{g^{t\phi} - [g^{tt}g^{\phi\phi} - (g^{t\phi})^2]\frac{\hat{L}_z}{g^{tt}\hat{H}_{\rm eff} - g^{t\phi}\hat{L}_z}}{g^{tt}E/M} \tag{A10b}$$

$$\dot{\theta} = \frac{\partial E}{\partial P_\theta} = -\frac{g^{\theta\theta}\hat{P}_\theta}{E/M(g^{tt}\hat{H}_{\rm eff} - g^{t\phi}\hat{L}_z).} \tag{A10c}$$

The parameters in the expressions of the coordinate-time frequencies ω_r, ω_θ, ω_ϕ [Eqs. (10a)–(10c)] are expressed by

$$K(k) = \int_0^{\pi/2}\frac{d\chi}{\sqrt{1-k\sin^2\chi}} \tag{A11a}$$

$$E(k) = \int_0^{\pi/2}\sqrt{1-k\sin^2\chi}d\chi \tag{A11b}$$

$$\Pi(z_-^2,k) = \int_0^{\pi/2}\frac{d\chi}{(1-z_-^2\sin^2\chi)\sqrt{1-k\sin^2\chi}} \tag{A11c}$$

$$X = \int_0^{\pi}\frac{ep\sin\xi}{(1+e\cos\xi)^2}\frac{d\xi}{\Delta_r P_r} \tag{A11d}$$

$$z_- = \cos\theta_{\min} \tag{A11e}$$

$$z_+ = \frac{L_z^2+Q+\beta+\sqrt{(L_z^2+Q+\beta)^2-4\beta Q}}{2\beta} \tag{A11f}$$

$$\beta^2 = a^2(\mu^2 - H_{\rm eff}^2) \tag{A11g}$$

$$k = z_-^2/z_+^2. \tag{A11h}$$

APPENDIX B: 2PN FLUXES

The hybrid scheme of fluxes proposed by Gair and Glampedakis [44] is given by

$$(\dot{L}_z)_{\rm mod} = (1-e^2)^{3/2}[(1-e^2)^{-3/2}(\dot{L}_z)_{\rm 2PN}(p,\iota,e,a) - (\dot{L}_z)_{\rm 2PN}(p,\iota,0,a) + (\dot{L}_z)_{\rm fit}] \tag{B1}$$

$$(\dot{Q})_{\rm mod} = (1-e^2)^{3/2}\sqrt{Q(p,\iota,e,a)}\left[(1-e^2)^{-3/2}\left(\frac{\dot{Q}}{\sqrt{Q}}\right)_{\rm 2PN}(p,\iota,e,a) - \left(\frac{\dot{Q}}{\sqrt{Q}}\right)_{\rm 2PN}(p,\iota,0,a) + 2\tan\iota\left((\dot{L}_z)_{\rm fit} + \frac{\sqrt{Q(p,\iota,0,a)}}{\sin^2\iota}(i)_{\rm fit}\right)\right] \tag{B2}$$

$$\dot{E} = (1-e^2)^{3/2}\left[(1-e^2)^{-3/2}(\dot{E})_{\rm 2PN}(p,\iota,e,a) - (\dot{E})_{\rm 2PN}(p,\iota,0,a) - \frac{N_4(p,\iota)}{N_1(p,\iota)}(\dot{L}_z)_{\rm fit}(p,\iota,0,a) - \frac{N_5(p,\iota)}{N_1(p,\iota)}(\dot{Q})_{\rm mod}(p,\iota,0,a)\right], \tag{B3}$$

with

$$(\dot{E})_{\rm 2PN} = -\frac{32}{5}\frac{\mu^2}{M^2}\left(\frac{M}{p}\right)^5(1-e^2)^{3/2}\left[\left(1+\frac{73e^2}{24}+\frac{37e^4}{96}\right)-q\left(\frac{M}{p}\right)^{3/2}\left(\frac{73}{12}+\frac{823}{24}e^2+\frac{949}{32}e^4+\frac{491}{192}e^6\right)\cos\iota\right.$$
$$-\left(\frac{M}{p}\right)\left(\frac{1247}{336}+\frac{9181}{672}e^2\right)+\pi\left(\frac{M}{p}\right)^{3/2}\left(4+\frac{1375}{48}\right)-\left(\frac{M}{p}\right)^2\left(\frac{44711}{9072}+\frac{172157}{2592}e^2\right)$$
$$\left.+q^2\left(\frac{M}{p}\right)^2\left(\frac{33}{16}+\frac{359}{32}e^2\right)-\frac{527}{96}q^2\left(\frac{M}{p}\right)^2\sin^2\iota\right] \tag{B4}$$

$$(\dot{L}_z)_{\rm 2PN} = -\frac{32}{5}\frac{\mu^2}{M}\left(\frac{M}{p}\right)^{7/2}(1-e^2)^{3/2}\left[\left(1+\frac{7}{8}e^2\right)\cos\iota+q\left(\frac{M}{p}\right)^{3/2}\left\{\left(\frac{61}{24}+\frac{63}{8}e^2+\frac{95}{64}e^4\right)\right.\right.$$
$$\left.\left.-\cos^2\iota\left(\frac{61}{8}+\frac{91}{4}e^2+\frac{461}{64}e^4\right)\right\}-\left(\frac{M}{p}\right)\left(\frac{1247}{336}+\frac{425}{36}e^2\right)\cos\iota+\pi\left(\frac{M}{p}\right)^{3/2}\left(4+\frac{97}{8}e^2\right)\cos\iota\right.$$
$$\left.-\left(\frac{M}{p}\right)^2\left(\frac{44711}{9072}+\frac{302893}{6048}e^2\right)\cos\iota+q^2\left(\frac{M}{p}\right)^2\cos\iota\left(\left(\frac{33}{16}+\frac{95}{16}e^2\right)-\frac{45}{8}\sin^2\iota\right)\right] \tag{B5}$$

$$\dot{Q} = -\frac{64}{5}\frac{\mu^2}{M}\left(\frac{M}{p}\right)^{7/2}\sqrt{Q}\sin\iota(1-e^2)^{3/2}\left[\left(1+\frac{7}{8}e^2\right)-q\left(\frac{M}{p}\right)^{3/2}\cos\iota\left(\frac{61}{8}+\frac{91}{4}e^2+\frac{461}{64}e^4\right)\right.$$
$$-\left(\frac{M}{p}\right)\left(\frac{1247}{336}+\frac{425}{36}e^2\right)+\pi\left(\frac{M}{p}\right)^{3/2}\left(4+\frac{97}{8}e^2\right)-\left(\frac{M}{p}\right)^2\left(\frac{44711}{9072}+\frac{302893}{6048}e^2\right)$$
$$\left.+q^2\left(\frac{M}{p}\right)^2\left(\left(\frac{33}{16}+\frac{95}{16}e^2\right)-\frac{45}{8}\sin^2\iota\right)\right] \tag{B6}$$

$$(\dot{L}_z)_{\rm fit} = -\frac{32}{5}\frac{\mu^2}{M}\left(\frac{M}{p}\right)^{7/2}\left[\cos\iota+q\left(\frac{M}{p}\right)^{3/2}\left(\frac{61}{24}-\frac{61}{8}\cos^2\iota\right)-\frac{1247}{336}\left(\frac{M}{p}\right)\cos\iota\right.$$
$$+4\pi\left(\frac{M}{p}\right)^{3/2}\cos\iota-\frac{44711}{9072}\left(\frac{M}{p}\right)^2\cos\iota+q^2\left(\frac{M}{p}\right)^2\cos\iota\left(\frac{33}{16}-\frac{45}{8}\sin^2\iota\right)$$
$$+\left(\frac{M}{p}\right)^{5/2}\left\{q\left(d_1^a+d_1^b\left(\frac{M}{p}\right)^{1/2}+d_1^c\left(\frac{M}{p}\right)\right)+q^3\left(d_2^a+d_2^b\left(\frac{M}{p}\right)^{1/2}+d_2^c\left(\frac{M}{p}\right)\right)\right.$$
$$+\cos\iota\left(c_1^a+c_1^b\left(\frac{M}{p}\right)^{1/2}+c_1^c\left(\frac{M}{p}\right)\right)+q^2\cos\iota\left(c_2^a+c_2^b\left(\frac{M}{p}\right)^{1/2}+c_2^c\left(\frac{M}{p}\right)\right)$$
$$+q^4\cos\iota\left(c_3^a+c_3^b\left(\frac{M}{p}\right)^{1/2}+c_3^c\left(\frac{M}{p}\right)\right)+q\cos^2\iota\left(c_4^a+c_4^b\left(\frac{M}{p}\right)^{1/2}+c_4^c\left(\frac{M}{p}\right)\right)$$
$$+q^3\cos^2\iota\left(c_5^a+c_5^b\left(\frac{M}{p}\right)^{1/2}+c_5^c\left(\frac{M}{p}\right)\right)+q^2\cos^3\iota\left(c_6^a+c_6^b\left(\frac{M}{p}\right)^{1/2}+c_6^c\left(\frac{M}{p}\right)\right)$$
$$+q^4\cos^3\iota\left(c_7^a+c_7^b\left(\frac{M}{p}\right)^{1/2}+c_7^c\left(\frac{M}{p}\right)\right)+q^3\cos^4\iota\left(c_8^a+c_8^b\left(\frac{M}{p}\right)^{1/2}+c_8^c\left(\frac{M}{p}\right)\right)$$
$$\left.+q^4\cos^5\iota\left(c_9^a+c_9^b\left(\frac{M}{p}\right)^{1/2}+c_9^c\left(\frac{M}{p}\right)\right)\right\}$$
$$+\left(\frac{M}{p}\right)^{7/2}q\cos\iota\left\{\left(f_1^a+f_1^b\left(\frac{M}{p}\right)^{1/2}\right)+q\left(f_2^a+f_2^b\left(\frac{M}{p}\right)^{1/2}\right)+q^2\left(f_3^a+f_3^b\left(\frac{M}{p}\right)^{1/2}\right)\right.$$
$$\left.\left.+\cos^2\iota\left(f_4^a+f_4^b\left(\frac{M}{p}\right)^{1/2}\right)+q\cos^2\iota\left(f_5^a+f_5^b\left(\frac{M}{p}\right)^{1/2}\right)+q^2\cos^2\iota\left(f_6^a+f_6^b\left(\frac{M}{p}\right)^{1/2}\right)\right\}\right] \tag{B7}$$

$$
\begin{aligned}
(i)_{\rm fit} = {} & \frac{32}{5}\frac{\mu^2}{M} q \frac{\sin^2\iota}{\sqrt{Q}} \left(\frac{M}{p}\right)^{5/2} \left[\frac{61}{24} + \left(\frac{M}{p}\right)\left(d_1^a + d_1^b\left(\frac{M}{p}\right)^{1/2} + d_1^c\left(\frac{M}{p}\right)\right) + q^2\left(\frac{M}{p}\right)\left(d_2^a + d_2^b\left(\frac{M}{p}\right)^{1/2} + d_2^c\left(\frac{M}{p}\right)\right)\right. \\
& + q\cos\iota\left(\frac{M}{p}\right)^{1/2}\left(c_{10}^a + c_{10}^b\left(\frac{M}{p}\right)^{1/2} + c_{10}^c\left(\frac{M}{p}\right)\right) + q^2\cos^2\iota\left(\frac{M}{p}\right)\left(c_{11}^a + c_{11}^b\left(\frac{M}{p}\right)^{1/2} + c_{11}^c\left(\frac{M}{p}\right)\right) \\
& + \left(\frac{M}{p}\right)^{5/2} q^3\cos\iota\left\{\left(f_7^a + f_7^b\left(\frac{M}{p}\right)^{1/2}\right) + q\left(f_8^a + f_8^b\left(\frac{M}{p}\right)^{1/2}\right)\right. \\
& \left.\left. + \cos^2\iota\left(f_9^a + f_9^b\left(\frac{M}{p}\right)^{1/2}\right) + q\cos^2\iota\left(f_{10}^a + f_{10}^b\left(\frac{M}{p}\right)^{1/2}\right)\right\}\right],
\end{aligned} \tag{B8}
$$

where

$$
\begin{aligned}
& d_1^a = -10.7420, \quad d_1^b = 28.5942, \quad d_1^c = -9.07738, \quad d_2^a = -1.42836, \quad d_2^b = 10.7003, \quad d_2^c = -33.7090, \\
& c_1^a = -28.1517, \quad c_1^b = 60.9607, \quad c_1^c = 40.9998, \quad c_2^a = -0.348161, \quad c_2^b = 2.37258, \quad c_2^c = -66.6584, \\
& c_3^a = -0.715392, \quad c_3^b = 3.21593, \quad c_3^c = 5.28888, \quad c_4^a = -7.61034, \quad c_4^b = 128.878, \quad c_4^c = -475.465, \\
& c_5^a = 12.2908, \quad c_5^b = -113.125, \quad c_5^c = 306.119, \quad c_6^a = 40.9259, \quad c_6^b = -347.271, \quad c_6^c = 886.503, \\
& c_7^a = -25.4831, \quad c_7^b = 224.227, \quad c_7^c = 490.982, \quad c_8^a = -9.00634, \quad c_8^b = 91.1767, \quad c_8^c = -297.002, \\
& c_9^a = -0.645000, \quad c_9^b = -5.13592, \quad c_9^c = 47.1982, \quad c_{10}^a = -0.0309341, \quad c_{10}^b = -22.2416, \quad c_{10}^c = 7.55265, \\
& c_{11}^a = -3.33476, \quad c_{11}^b = 22.7013, \quad c_{11}^c = -12.4700, \quad f_1^a = -283.955, \quad f_1^b = 736.209, \quad f_2^a = 483.266, \\
& f_2^b = -1325.19, \quad f_3^a = -219.224, \quad f_3^b = 634.499, \quad f_4^a = -25.8203, \quad f_4^b = 82.0780, \quad f_5^a = 301.478, \\
& f_5^b = -904.161, \quad f_6^a = -271.966, \quad f_6^b = 827.319, \quad f_7^a = -162.268, \quad f_7^b = 247.168, \quad f_8^a = 152.125, \\
& f_8^b = -182.165, \quad f_9^a = 184.465, \quad f_9^b = -267.553, \quad f_{10}^a = -188.132, \quad f_{10}^b = 254.067.
\end{aligned} \tag{B9}
$$

However, the mass-ratio correction is not involved in the expressions of their 2PN fluxes. In this work, we make some corresponding improvements by adding mass-ratio correction terms in Eqs. (B4)–(B6) to get the evolution expressions of orbit parameters (p, e, ι). Our improved 2PN fluxes are given by [26,43,66]

$$
\begin{aligned}
(\dot{E})_{\rm 2PN} = {} & -\frac{32}{5}\frac{\mu^2}{M^2}\left(\frac{M}{p}\right)^5 (1-e^2)^{3/2}\left[\left(1 + \frac{73e^2}{24} + \frac{37e^4}{96}\right) - q\left(\frac{M}{p}\right)^{3/2}\left(\frac{73}{12} + \frac{823}{24}e^2 + \frac{949}{32}e^4 + \frac{491}{192}e^6\right)\cos\iota\right. \\
& - \left(\frac{M}{p}\right)\left(\frac{1247}{336} + \frac{5\nu}{4} + e^2\left(\frac{9181}{672} + \frac{325\nu}{24}\right) - e^4\left(\frac{809}{128} - \frac{435\nu}{32}\right) - e^6\left(\frac{8609}{5376} - \frac{185\nu}{192}\right)\right) \\
& \left. + \pi\left(\frac{M}{p}\right)^{3/2}\left(4 + \frac{1375}{48}\right) - \left(\frac{M}{p}\right)^2\left(\frac{44711}{9072} + \frac{172157}{2592}e^2\right) + q^2\left(\frac{M}{p}\right)^2\left(\frac{33}{16} + \frac{359}{32}e^2\right) - \frac{527}{96}q^2\left(\frac{M}{p}\right)^2\sin^2\iota\right]
\end{aligned} \tag{B10}
$$

$$
\begin{aligned}
(\dot{L}_z)_{\rm 2PN} = {} & -\frac{32\mu^2}{5\,M}\left(\frac{M}{p}\right)^{7/2}(1-e^2)^{3/2}\left[\left(1 + \frac{7}{8}e^2\right)\cos\iota + q\left(\frac{M}{p}\right)^{3/2}\left\{\left(\frac{61}{24} + \frac{63}{8}e^2 + \frac{95}{64}e^4\right)\right.\right. \\
& \left.\left. - \cos^2\iota\left(\frac{61}{8} + \frac{91}{4}e^2 + \frac{461}{64}e^4\right)\right\} - \left(\frac{M}{p}\right)\left(\frac{1247}{336} + \frac{7\nu}{4} + e^2\left(\frac{425}{36} + \frac{401\nu}{48}\right) - e^4\left(\frac{10751}{2688} - \frac{205\nu}{96}\right)\right)\cos\iota \right. \\
& \left. + \pi\left(\frac{M}{p}\right)^{3/2}\left(4 + \frac{97}{8}e^2\right)\cos\iota - \left(\frac{M}{p}\right)^2\left(\frac{44711}{9072} + \frac{302893}{6048}e^2\right)\cos\iota + q^2\left(\frac{M}{p}\right)^2\cos\iota\left(\left(\frac{33}{16} + \frac{95}{16}e^2\right) - \frac{45}{8}\sin^2\iota\right)\right]
\end{aligned} \tag{B11}
$$

$$\dot{Q} = -\frac{64}{5}\frac{\mu^2}{M}\left(\frac{M}{p}\right)^{7/2}\sqrt{Q}\sin\iota(1-e^2)^{3/2}\left[\left(1+\frac{7}{8}e^2\right) - q\left(\frac{M}{p}\right)^{3/2}\cos\iota\left(\frac{61}{8}+\frac{91}{4}e^2+\frac{461}{64}e^4\right)\right.$$
$$-\left(\frac{M}{p}\right)\left(\frac{1247}{336}+\frac{7\nu}{4}+e^2\left(\frac{425}{36}+\frac{401\nu}{48}\right)-e^4\left(\frac{10751}{2688}-\frac{205\nu}{96}\right)\right)+\pi\left(\frac{M}{p}\right)^{3/2}\left(4+\frac{97}{8}e^2\right)-\left(\frac{M}{p}\right)^2\left(\frac{44711}{9072}\right.$$
$$\left.\left.+\frac{302893}{6048}e^2\right)+q^2\left(\frac{M}{p}\right)^2\left(\left(\frac{33}{16}+\frac{95}{16}e^2\right)-\frac{45}{8}\sin^2\iota\right)\right]. \tag{B12}$$

Our final hybrid scheme of fluxes is given by Eqs. (B1)–(B3) with Eqs. (B7)–(B8) and Eqs. (B10)–(B12).

[1] P. Amaro-Seoane, J. R. Gair, M. Freitag, M. C. Miller, I. Mandel, C. J. Cutler, and S. Babak, Intermediate and extreme mass-ratio inspirals—astrophysics, science applications and detection using LISA, Classical Quantum Gravity **24**, R113 (2007).

[2] S. Babak, J. Gair, A. Sesana, E. Barausse, C. F. Sopuerta, C. P. L. Berry, E. Berti, P. Amaro-Seoane, A. Petiteau, and A. Klein, Science with the space-based interferometer LISA. V. Extreme mass-ratio inspirals, Phys. Rev. D **95**, 103012 (2017).

[3] K. Danzmann *et al.*, LISA Laser Interferometer Space Antenna A proposal in response to the ESA call for L 3 mission concepts Lead (2017), https://api.semanticscholar.org/CorpusID:62787610.

[4] W. Rui Hu and Y.-L. Wu, The Taiji program in space for gravitational wave physics and the nature of gravity, Natl. Sci. Rev. **4**, 685 (2017).

[5] X. Zhong, W.-B. Han, Z. Luo, and Y. Wu, Exploring the nature of black hole and gravity with an imminent merging binary of supermassive black holes, Sci. China Phys. Mech. Astron. **66**, 230411 (2023).

[6] J. Luo, L.-S. Chen, H.-Z. Duan, Y.-G. Gong, S. Hu, J. Ji, Q. Liu, J. Mei, V. Milyukov, M. Sazhin, C.-G. Shao, V. T. Toth, H.-B. Tu, Y. Wang, Y. Wang, H.-C. Yeh, M.-S. Zhan, Y. Zhang, V. Zharov, and Z.-B. Zhou, Tianqin: A space-borne gravitational wave detector, Classical Quantum Gravity **33**, 035010 (2016).

[7] A. R. King, S. Lubow, G. Ogilvie, and J. Pringle, Aligning spinning black holes and accretion discs, Mon. Not. R. Astron. Soc. **363**, 49 (2005).

[8] S. A. Hughes and R. D. Blandford, Black hole mass and spin coevolution by mergers, Astrophys. J. **585**, L101 (2003).

[9] M. J. Rees and M. Volonteri, *Massive Black Holes: Formation and Evolution* (Cambridge University Press, 2006), 10.1017/S1743921307004681.

[10] Y. Wang, F. Wang, Y. Zou, and Z. Dai, A bright electromagnetic counterpart to extreme mass ratio inspirals, Astrophys. J. Lett. **886**, L22 (2019).

[11] B. F. Schutz, Determining the Hubble constant from gravitational wave observations, Nature (London) **323**, 310 (1986).

[12] C. L. MacLeod and C. J. Hogan, Precision of Hubble constant derived using black hole binary absolute distances and statistical redshift information, Phys. Rev. D **77**, 043512 (2008).

[13] Z. Y. Zhao, Y. Y. Wang, Y. C. Zou, F. Y. Wang, and Z. G. Dai, Quasi-periodic eruptions from the helium envelope of hydrogen-deficient stars stripped by supermassive black holes, Astron. Astrophys. **661**, A55 (2022).

[14] J. R. Gair, M. Vallisneri, S. L. Larson, and J. G. Baker, Testing general relativity with low-frequency, space-based gravitational-wave detectors, Living Rev. Relativity **16**, 7 (2013).

[15] L. Barack and C. Cutler, Using LISA extreme-mass-ratio inspiral sources to test off-Kerr deviations in the geometry of massive black holes, Phys. Rev. D **75**, 042003 (2007).

[16] F. D. Ryan, Accuracy of estimating the multipole moments of a massive body from the gravitational waves of a binary inspiral, Phys. Rev. D **56**, 1845 (1997).

[17] N. A. Collins and S. A. Hughes, Towards a formalism for mapping the spacetimes of massive compact objects: Bumpy black holes and their orbits, Phys. Rev. D **69**, 124022 (2004).

[18] K. Fransen and D. R. Mayerson, Detecting equatorial symmetry breaking with LISA, Phys. Rev. D **106**, 064035 (2022).

[19] S. Xin, W.-B. Han, and S.-C. Yang, Gravitational waves from extreme-mass-ratio inspirals using general parametrized metrics, Phys. Rev. D **100**, 084055 (2019).

[20] T. Hinderer and E. E. Flanagan, Two-timescale analysis of extreme mass ratio inspirals in Kerr spacetime: Orbital motion, Phys. Rev. D **78**, 064028 (2008).

[21] L. Barack and A. Pound, Self-force and radiation reaction in general relativity, Rep. Prog. Phys. **82**, 016904 (2018).

[22] S. A. Hughes, Adiabatic and post-adiabatic approaches to extreme mass ratio inspiral, in *Fourteenth Marcel Grossmann Meeting—MG14*, edited by M. Bianchi, R. T. Jansen, and R. Ruffini (World Scientific Publishing, Singapore, 2018), pp. 1953–1959, 10.1142/9789813226609_0208.

[23] B. Wardell, A. Pound, N. Warburton, J. Miller, L. Durkan, and A. L. Tiec, Gravitational Waveforms for Compact Binaries from Second-Order Self-Force Theory, Phys. Rev. Lett. **130**, 241402 (2023).

[24] A. Pound, Accurately modelling extreme-mass-ratio inspirals: Beyond the geodesic approximation, https://pdf.pirsa.org/files/20010087.pdf (2020).

[25] S. A. Teukolsky, Perturbations of a rotating black hole. I. Fundamental equations for gravitational, electromagnetic, and neutrino-field perturbations, Astrophys. J. **185**, 635 (1973).
[26] N. Sago and R. Fujita, Calculation of radiation reaction effect on orbital parameters in Kerr spacetime, Prog. Theor. Exp. Phys. **2015**, 073E03 (2015).
[27] L. Barack and C. Cutler, LISA capture sources: Approximate waveforms, signal-to-noise ratios, and parameter estimation accuracy, Phys. Rev. D **69**, 082005 (2004).
[28] S. Babak, H. Fang, J. R. Gair, K. Glampedakis, and S. A. Hughes, "Kludge" gravitational waveforms for a test-body orbiting a Kerr black hole, Phys. Rev. D **75**, 024005 (2007).
[29] A. J. K. Chua, M. L. Katz, N. Warburton, and S. A. Hughes, Rapid Generation of Fully Relativistic Extreme-Mass-Ratio-Inspiral Waveform Templates for LISA Data Analysis, Phys. Rev. Lett. **126**, 051102 (2021).
[30] S. A. Hughes, N. Warburton, G. Khanna, A. J. K. Chua, and M. L. Katz, Adiabatic waveforms for extreme mass-ratio inspirals via multivoice decomposition in time and frequency, Phys. Rev. D **103**, 104014 (2021).
[31] N. Yunes, A. Buonanno, S. A. Hughes, M. C. Miller, and Y. Pan, Modeling Extreme Mass Ratio Inspirals within the Effective-One-Body Approach, Phys. Rev. Lett. **104**, 091102 (2010).
[32] W.-B. Han and Z. Cao, Constructing effective one-body dynamics with numerical energy flux for intermediate-mass-ratio inspirals, Phys. Rev. D **84**, 044014 (2011).
[33] W.-B. Han, Z. Cao, and Y.-M. Hu, Excitation of high frequency voices from intermediate-mass-ratio inspirals with large eccentricity, Classical Quantum Gravity **34**, 225010 (2017).
[34] W.-B. Han, Gravitational waves from extreme-mass-ratio inspirals in equatorially eccentric orbits, Int. J. Mod. Phys. D **23**, 1450064 (2014).
[35] N. Yunes, A. Buonanno, S. A. Hughes, Y. Pan, E. Barausse, M. C. Miller, and W. Throwe, Extreme mass-ratio inspirals in the effective-one-body approach: Quasicircular, equatorial orbits around a spinning black hole, Phys. Rev. D **83**, 044044 (2011).
[36] A. J. Chua, C. J. Moore, and J. R. Gair, Augmented kludge waveforms for detecting extreme-mass-ratio inspirals, Phys. Rev. D **96**, 044005 (2017).
[37] P. D. D'Eath, Interaction of two black holes in the slow-motion limit, Phys. Rev. D **12**, 2183 (1975).
[38] K. Arun, S. Babak, E. Berti, N. Cornish, C. Cutler, J. Gair, S. A. Hughes, B. R. Iyer, R. N. Lang, I. Mandel *et al.*, Massive black-hole binary inspirals: Results from the LISA parameter estimation taskforce, Classical Quantum Gravity **26**, 094027 (2009).
[39] E. Huerta and J. R. Gair, Influence of conservative corrections on parameter estimation for extreme-mass-ratio inspirals, Phys. Rev. D **79**, 084021 (2009).
[40] C. J. Moore, E. Finch, R. Buscicchio, and D. Gerosa, Testing general relativity with gravitational-wave catalogs: The insidious nature of waveform systematics, Iscience **24**, 102577 (2021).
[41] Q. Hu and J. Veitch, Accumulating errors in tests of general relativity with gravitational waves: Overlapping signals and inaccurate waveforms, Astrophys. J. **945**, 103 (2023).
[42] C. Zhang, W.-B. Han, X.-Y. Zhong, and G. Wang, Geometrized effective-one-body formalism for extreme-mass-ratio limits: Generic orbits, Phys. Rev. D **104**, 024050 (2021).
[43] C. Zhang, W.-B. Han, and S.-C. Yang, Analytical effective one-body formalism for extreme-mass-ratio inspirals with eccentric orbits, Commun. Theor. Phys. **73**, 085401 (2021).
[44] J. R. Gair and K. Glampedakis, Improved approximate inspirals of test bodies into Kerr black holes, Phys. Rev. D **73**, 064037 (2006).
[45] T. Damour, Coalescence of two spinning black holes: An effective one-body approach, Phys. Rev. D **64**, 124013 (2001).
[46] A. Buonanno and T. Damour, Effective one-body approach to general relativistic two-body dynamics, Phys. Rev. D **59**, 084006 (1999).
[47] E. Barausse and A. Buonanno, Extending the effective-one-body Hamiltonian of black-hole binaries to include next-to-next-to-leading spin-orbit couplings, Phys. Rev. D **84**, 104027 (2011).
[48] E. Barausse and A. Buonanno, Improved effective-one-body Hamiltonian for spinning black-hole binaries, Phys. Rev. D **81**, 084024 (2010).
[49] L. Rezzolla, E. Barausse, E. N. Dorband, D. Pollney, C. Reisswig, J. Seiler, and S. Husa, Final spin from the coalescence of two black holes, Phys. Rev. D **78**, 044002 (2008).
[50] E. Barausse and L. Rezzolla, Predicting the direction of the final spin from the coalescence of two black holes, Astrophys. J. **704**, L40 (2009).
[51] J. Steinhoff, T. Hinderer, A. Buonanno, and A. Taracchini, Dynamical tides in general relativity: Effective action and effective-one-body Hamiltonian, Phys. Rev. D **94**, 104028 (2016).
[52] J. Healy, J. Levin, and D. Shoemaker, Zoom-Whirl Orbits in Black Hole Binaries, Phys. Rev. Lett. **103**, 131101 (2009).
[53] K. Glampedakis and D. Kennefick, Zoom and whirl: Eccentric equatorial orbits around spinning black holes and their evolution under gravitational radiation reaction, Phys. Rev. D **66**, 044002 (2002).
[54] A. Nagar and S. Albanesi, Toward a gravitational self-force-informed effective-one-body waveform model for nonprecessing, eccentric, large-mass-ratio inspirals, Phys. Rev. D **106**, 064049 (2022).
[55] A. Albertini, A. Nagar, A. Pound, N. Warburton, B. Wardell, L. Durkan, and J. Miller, Comparing second-order gravitational self-force and effective one body waveforms from inspiralling, quasicircular and nonspinning black hole binaries. II. The large-mass-ratio case, Phys. Rev. D **106**, 084062 (2022).
[56] J. Mathews, A. Pound, and B. Wardell, Self-force calculations with a spinning secondary, Phys. Rev. D **105**, 084031 (2022).
[57] S. A. Teukolsky, Rotating Black Holes: Separable Wave Equations for Gravitational and Electromagnetic Perturbations, Phys. Rev. Lett. **29**, 1114 (1972).
[58] Y. Mino, M. Sasaki, M. Shibata, H. Tagoshi, and T. Tanaka, Chapter 1. Black hole perturbation, Prog. Theor. Phys. Suppl. **128**, 1 (1997).

[59] R. Fujita and H. Tagoshi, New numerical methods to evaluate homogeneous solutions of the Teukolsky equation. II:—Solutions of the continued fraction equation, Prog. Theor. Phys. **113**, 1165 (2005).
[60] G. A. Piovano, A. Maselli, and P. Pani, Extreme mass ratio inspirals with spinning secondary: A detailed study of equatorial circular motion, Phys. Rev. D **102**, 024041 (2020).
[61] S. A. Teukolsky and W. H. Press, Perturbations of a rotating black hole. III. Interaction of the hole with gravitational and electromagnetic radiation, Astrophys. J. **193**, 443 (1974).
[62] A. Pound and B. Wardell, Black hole perturbation theory and gravitational self-force, in *Handbook of Gravitational Wave Astronomy* (Springer, Singapore, 2021), pp. 1–119, 10.1007/978-981-15-4702-7_38-1.
[63] Black hole perturbation club (b. h. p. c.), https://sites.google.com/view/bhpc1996/home (1996).
[64] S. Isoyama, R. Fujita, A. J. K. Chua, H. Nakano, A. Pound, and N. Sago, Adiabatic Waveforms from Extreme-Mass-Ratio Inspirals: An Analytical Approach, Phys. Rev. Lett. **128**, 231101 (2022).
[65] R. Fujita, W. Hikida, and H. Tagoshi, An efficient numerical method for computing gravitational waves induced by a particle moving on eccentric inclined orbits around a Kerr black hole, Prog. Theor. Phys. **121**, 843 (2009).
[66] T. Hinderer and S. Babak, Foundations of an effective-one-body model for coalescing binaries on eccentric orbits, Phys. Rev. D **96**, 104048 (2017).
[67] L. S. Finn, Detection, measurement, and gravitational radiation, Phys. Rev. D **46**, 5236 (1992).
[68] S. L. Larson, Online sensitivity curve generator, http://www.srl.caltech.edu/ shane/sensitivity/MakeCurve.html (2002).
[69] T. A. Prince, M. Tinto, S. L. Larson, and J. W. Armstrong, LISA optimal sensitivity, Phys. Rev. D **66**, 122002 (2002).
[70] A. Nitz *et al.*, gwastro/pycbc: v2.0.5 release of pycbc (2022), https://zenodo.org/record/6912865.
[71] E. Battista and V. De Falco, First post-Newtonian generation of gravitational waves in Einstein-Cartan theory, Phys. Rev. D **104**, 084067 (2021).
[72] E. Battista and V. D. Falco, Gravitational waves at the first post-Newtonian order with the Weyssenhoff fluid in Einstein–Cartan theory, Eur. Phys. J. C **82**, 628 (2022).
[73] S. Vitale and W. Del Pozzo, How serious can the stealth bias be in gravitational wave parameter estimation?, Phys. Rev. D **89**, 022002 (2014).
[74] M. Isi, K. Chatziioannou, and W. M. Farr, Hierarchical Test of General Relativity with Gravitational Waves, Phys. Rev. Lett. **123**, 121101 (2019).